Improvement of Operational Airborne Gamma Radiation Snow Water Equivalent Estimates using SMAP Soil Moisture

Eunsang Cho[1,2*], Jennifer M. Jacobs[1,2], Ronny Schroeder[2†], Samuel E. Tuttle[3], Carrie Olheiser[4]

[1] Department of Civil and Environmental Engineering, University of New Hampshire, Durham, NH, USA
[2] Earth Systems Research Center, Institute for the Study of Earth, Oceans, and Space, University of New Hampshire, Durham, NH, USA
[3] Mount Holyoke College, South Hadley, MA, USA
[4] NOAA National Weather Service Office of Water Prediction, Chanhassen, MN, USA

[†] Ronny Schroeder's current affiliation is the Applied Aviation Sciences Department, Embry-Riddle Aeronautical University, Prescott, AZ, USA

[*]Corresponding author: Eunsang Cho (ec1072@wildcats.unh.edu)

Highlights

- The NOAA airborne gamma radiation surveys provide unique SM and SWE records
- Airborne gamma SWE estimate biases result when SM changed after fall SM surveys
- SMAP SM has the best agreement with gamma SM as compared to other SM products
- Operational gamma SWE improved by updating antecedent SM prior to freeze onset
- SMAP-updated SWE showed better agreement with two independent SWE observations

3rd Revision Submitted to *Remote Sensing of Environment*

January 13, 2020

Abstract

Knowledge of snow water equivalent (SWE) magnitude and spatial distribution are keys to improving snowmelt flood predictions. Since the 1980s, the operational National Oceanic and Atmospheric Administration's (NOAA) airborne gamma radiation soil moisture (SM) and SWE survey has provided over 20,000 SWE observations to regional National Weather Service (NWS) River Forecast Centers (RFCs). Because the gamma SWE algorithm is based on the difference in natural gamma emission measurements from the soil between bare (fall) and snow-covered (winter) conditions, it requires a baseline fall SM for each flight line. The operational approach assumes the fall SM remains constant throughout that winter's SWE survey. However, early-winter snowmelt and rainfall events after the fall SM surveys have the potential to introduce large biases into airborne gamma SWE estimates. In this study, operational airborne gamma radiation SWE measurements were improved by updating the baseline fall SM with Soil Moisture Active Passive (SMAP) enhanced SM measurements immediately prior to winter onset over the north-central and eastern United States and southern Canada from September 2015 to April 2018. The operational airborne gamma SM had strong agreement with the SMAP SM (Pearson's correlation coefficient, R = 0.69, unbiased root mean square difference, ubRMSD = 0.057 m^3/m^3), compared to the Advanced Microwave Scanning Radiometer 2 (AMSR2) SM (R = 0.45, ubRMSD = 0.072 m^3/m^3) and the North American Land Data Assimilation System Phase 2 (NLDAS-2) Mosaic SM products (R = 0.53, ubRMSD = 0.069 m^3/m^3) in non-forested regions. The SMAP-enhanced gamma SWE was evaluated with satellite-based SWE (R = 0.57, ubRMSD = 34 mm) from the Special Sensor Microwave Imager Sounder (SSMIS) and in-situ SWE (R = 0.71 - 0.96) from the Soil Climate Analysis Network and United States Army Corps of Engineer (USACE) St. Paul District, which had better agreement than the operational gamma SWE (R =

0.48, ubRMSD = 36 mm for SSMIS and R = 0.65 - 0.75 for in-situ SWE). The results contribute to improving snowmelt flood predictions as well as the accuracy of the NOAA SNOw Data Assimilation System.

Keywords

Snow water equivalent, Airborne gamma radiation, Soil moisture, SSMIS, SMAP, AMSR2, NLDAS-2

1 Introduction

In snowmelt-dominated regions, water resources management and flood predictions rely on accurate snowpack measurements (De Roo et al., 2003; Liu et al., 2012). The most important snowpack measure for streamflow prediction is snow water equivalent (SWE), which is the depth of liquid water that would result if the entire snowpack melted (Bergeron et al., 2016). In the north-central U.S. and southern Canada, accurate flood predictions are needed to help communities prepare for flood events and allocate flood management resources. However, flood prediction is hampered by insufficient information about the magnitude and spatial distribution of SWE and snowmelt across the landscape (Tuttle et al., 2017; Schroeder et al., 2019). In the flood-prone Red River of the North in Minnesota and North Dakota in U.S and Manitoba in Canada (Rannie, 2015; Stadnyk et al., 2016; Todhunter, 2001; Wazney and Clark, 2015), the National Weather Service (NWS) North Central River Forecasting Center (NCRFC) overestimated a peak flow by 70% of the observed 2013 flow in the region. The flood forecasters indicate that uncertainties in SWE spatial distribution as well as antecedent soil moisture estimates were potential causes of the forecasting's failure (personnel communication, Mike DeWeese NOAA NCRFC).

Since the late 1970s, satellite passive microwave sensors such as the Scanning Multichannel Microwave Radiometer (SMMR) aboard the NASA Nimbus-7 satellite (temporal coverage: 1978 – 1987), and the Special Sensor Microwave/Imager (SSM/I) and SSMIS aboard the Defense Meteorological Satellite Program (DMSP) series of satellites (F8, F11, F13, and F17: 1987 – current) have provided useful snowpack information globally (Armstrong et al., 1994; Derksen et al., 2005; Foster et al., 2005; Pulliainen and Hallikainen, 2001; Tait, 1998). The Advanced Microwave Scanning Radiometer for Earth Observing System (AMSR-E) aboard the

NASA Aqua satellite and AMSR2, a follow-on instrument of AMSR-E onboard the Japan Aerospace Exploration Agency (JAXA) Global Change Observation Mission 1-Water (GCOM-W1) satellite, have successfully provided snow depth and SWE for the past two decades (Dai et al., 2012; Kelly et al., 2003; Kelly, 2009; Cho et al., 2017). SWE from current satellite-based microwave sensors has proven to be a valuable asset for improving snowmelt streamflow predictions at a watershed scale (approximately 47,000 km^2; Vuyovich and Jacobs, 2011). Accurate SWE information at smaller scales remains challenging due to the coarse spatial resolution (e.g. 25 km by 25 km; 625 km^2) of passive microwave satellite observations. In addition, wet snow and variations in snow grain size make the microwave satellite retrieval of SWE difficult (Armstrong et al., 1993; Tuttle et al., 2017; Vuyovich et al., 2017).

Snow observations from airborne platforms can fill the knowledge gap between ground and satellite microwave remote sensing observations of snow (Painter et al., 2016). Airborne gamma-ray spectrometry supports operational snowpack monitoring efforts (Bland et al., 1997; Carroll, 2001; Grasty, 1982; Ishizaki et al., 2016). Since the 1980s, airborne gamma radiation snow surveys conducted by the NOAA's Office of Water Prediction (OWP; and formerly by the National Operational Hydrologic Remote Sensing Center [NOHRSC]) have provided SWE observations to regional NWS RFCs across the U.S. (Carroll, 2001; Mote et al., 2003). The historical 40 years gamma SWE record was proven as reliable long-term reference SWE observations across the U.S. and southern Canada (Cho et al., 2019). The SWE data are also assimilated into NOAA NWS's NOHRSC SNOw Data Assimilation System (SNODAS) (Barrett, 2003; Clow et al., 2012; Hedrick et al., 2015).

Terrestrial gamma-ray emission from radioisotopes in surface soils (~ top 20 cm) is attenuated by water in the liquid or solid form (Carroll, 2001; Peck et al., 1980). The difference

between gamma radiation measurements taken in the fall (without snow) and in the winter (with snow) forms the basis of gamma-ray based airborne SWE measurements. Each flight line's footprint is approximately 4.5 – 6 km^2 (15 – 20 km long and about 300 m wide). Flight lines are measured once in the fall (in October or November) and then revisited several times throughout the winter (January to April) to estimate SWE (Carroll, 2001). The operational gamma SWE measurements are considered to be accurate assuming that SM conditions measured during the fall survey remain unchanged prior to winter surveys. However, SM conditions can change due to late-season rainfall events and early-winter snowmelt, which can result in large gamma SWE errors (e.g. NASA SnowEx Science Plan; Durand et al., 2019). Tuttle et al. (2018), for example, found a root mean square difference of 42.7 mm between AMSR-E SWE and airborne gamma SWE in the Northern Great Plains, including parts of the North Dakota, South Dakota, Minnesota, and Iowa, the United States and southern Canadian prairies. They mentioned that a large portion of the error was likely due to the assumption that SM remains constant from fall into winter.

Beginning with the SMMR from 1978 to 1987, satellite active and passive microwave sensors such as AMSR-E (2002 – 2011), ASCAT (Advanced Scatterometer; 2007, 2012, and 2018 – present, from Metop-A, B, and C, respectively) and SMOS (Soil Moisture and Ocean Salinity; 2010 – present) have provided surface SM. Two recent instruments are the AMSR2 (2012 – present) and SMAP (Soil Moisture Active Passive; 2015 - present). The L-band radiometer aboard the National Aeronautics and Space Administration's (NASA) SMAP satellite is well suited for measuring surface SM (Entekhabi et al., 2010). SMAP was launched in January 2015 and provides SM measurements globally every 2-3 days. SMAP SM observations have been used to study soil moisture dynamics (Akbar et al., 2018; Kim et al., 2019; McColl et al.,

145 2017), which are important for hydrological and agricultural applications, such as flood detection
146 (Fournier et al., 2016), irrigation signals (Lawston et al., 2017), and drought monitoring (Mishra
147 et al., 2017), at both global and regional scales. However, satellite microwave-based SM
148 products have well-known limitations for representative depths (~ upper few centimeters) and
149 high uncertainties over dense-vegetated areas (Jackson & Schmugge, 1991; Entekhabi et al.
150 2014; Chan et al., 2018).

151 The physics used to estimate SM differ between gamma radiation and satellite microwave
152 sensing. The gamma radiation method uses the difference between the naturally occurring
153 terrestrial gamma radiation flux from wet and dry soils (Carroll, 1981; Jones & Carroll, 1983).
154 The gamma flux from the ground is a function of the water mass and constant radioisotope
155 concentration near the surface. The mass of the moisture regardless of any phase of water affects
156 the attenuation. Increasing SM increases the gamma radiation flux attenuation and decreases the
157 gamma flux at the ground surface. Passive microwave sensors estimate the soil dielectric
158 constant using the observed brightness temperature (Tb) of the land surface (Jackson et al.,
159 1993). Using the estimated dielectric constant, a dielectric mixing model leverages the large
160 difference between the dielectric constants of the soil particles (~4) and water (~80) to obtain the
161 amount of SM with soil texture information. In the single channel algorithm (SCA) in the NASA
162 SMAP standard products, the vertically polarized Tb observations by SMAP L-band are
163 converted to emissivity using ancillary physical temperature (Chan et al., 2018; Dong et al.,
164 2018; O'Neill et al., 2015; updated 2019). The derived emissivity is corrected for surface
165 roughness and vegetation to obtain soil emissivity. The soil emissivity is related to the dielectric
166 properties of the soil and the incidence angle. The Fresnel reflection equation (Ulaby et al., 1986)
167 is then used to determine the dielectric constant.

Land surface model (LSM) provides an alternative source of simulated SM products and have been vetted in weather and climate models as well as hydrological extreme monitoring (e.g. drought and floods) (Koster et al., 2009). The North American Land Data Assimilation System Phase 2 (NLDAS-2) provides simulated SM products for central North America using four land surface models, Noah (Ek et al., 2003; Wood et al., 1997), Mosaic (Koster and Suarez, 1996), Sacramento soil moisture accounting (SAC, Burnash, 1995), and the Variable Infiltration Capacity (VIC, Liang et al., 1994), which have high spatial (12.5 km by 12.5 km) and temporal (hourly) resolution (Xia et al., 2014).

This study seeks to identify which of the aforementioned SM products can improve airborne gamma SWE estimates by updating the ("baseline") fall operational gamma SM estimates to account for changes in SM conditions after baseline gamma flights. This study aims to answer the following four research questions:

1. Are temporal changes in SM from satellite and LSM model products similar to each other after baseline gamma flights?
2. Which satellite and LSM SM products have strong agreement with operational airborne gamma SM?
3. How much does updating the baseline operational gamma SM change gamma SWE estimates?
4. Does the updated gamma SWE improve agreement with independent SWE observations?

2 Study Concept

Operational airborne gamma radiation snow surveys rely on the assumption that the SM measured during the fall survey remains constant prior to winter SWE surveys. When SM

conditions evolve due to drying, rainfall events, and/or early-winter snowmelt, gamma SWE estimates biases result. Figure 1 shows an example of a SMAP soil moisture time series from the "ND440" flight line footprint, the gamma SM estimate for the flight line, and the daily rainfall and soil temperature data in Mooreton, North Dakota from North Dakota Agricultural Weather Network (NDAWN, https://ndawn.ndsu.nodak.edu) are also shown. The figure illustrates the soil moisture changes after the fall baseline gamma SM survey and their potential influence on the winter gamma SWE estimates. From the 9 November 2016 baseline gamma SM survey, SMAP SM evolves until 1 December 2017 with a net 0.12 m^3/m^3 increase. The gamma SWE estimated on 18 January 2017 using the baseline gamma SM value attributes all the additional gamma radiation attenuation in the winter measurement to SWE rather than accounting for the increase in soil moisture post-baseline survey. If the baseline gamma SM were updated to reflect the fall SM changes, then the operational gamma SWE should be reduced to reflect that portion of the attenuation of gamma radiation due to an increase in SM. Thus, gamma SWE estimates may be improved using an updated gamma SM estimate.

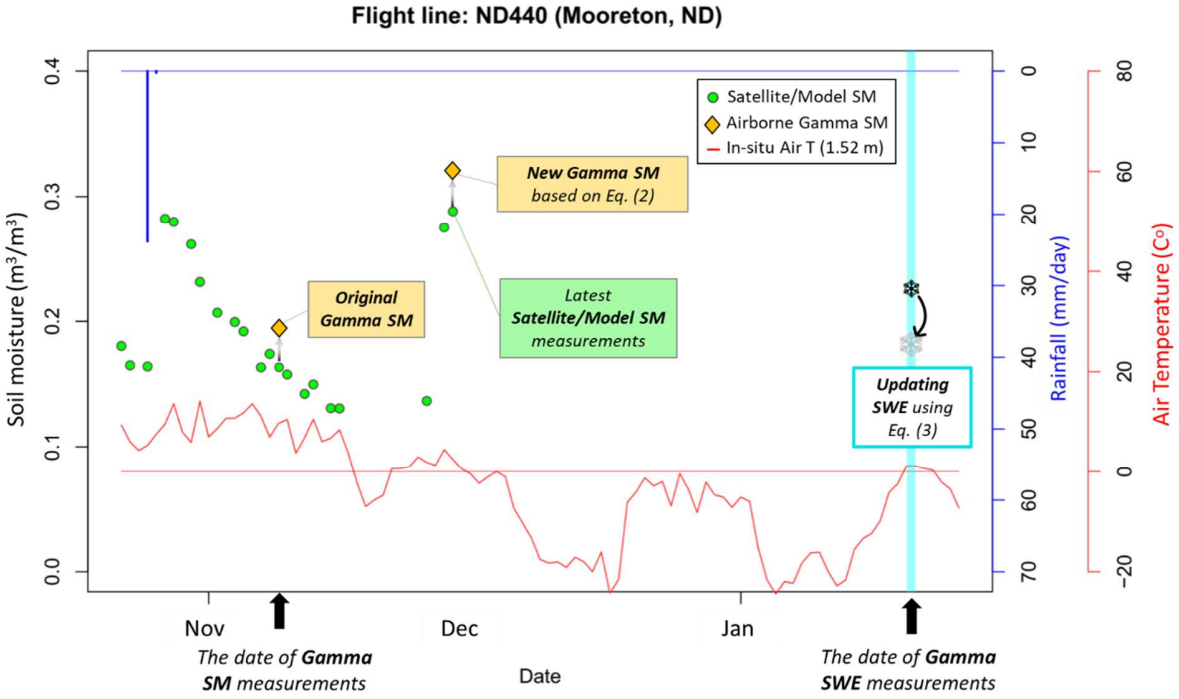

Figure 1. An example time series of satellite/model soil moisture (SMAP enhanced products in this figure) within the given flight line footprint and NOAA operational gamma soil moisture along with daily rainfall and air temperature in 2016 to 2017 from a North Dakota Agricultural Weather Network (NDAWN) station at Mooreton, ND. The ND440 flight line was flown over the Mooreton station. The increase in SMAP soil moisture in December was due to early snowmelt from 26 to 30, November. The errors of the SMAP product (ubRMSE < 0.04 m^3/m^3) meet the mission performance criteria from previous studies (Chen et al., 2018; Colliander et al., 2018).

3 Study Area

The study area comprises parts of the north-central and northeast United States and southern Canada (Figure 2), including parts of four RFCs (Missouri Basin RFC (MBRFC), North-Central RFC (NCRFC), North-East RFC (NERFC), and Mid-Atlantic RFC (MARFC)) and two Canadian Provinces including Saskatchewan (SK) and Manitoba (Winnipeg). The RFC boundaries (black lines) were designated by the NOAA NWS Integrated Hydrologic Automated Basin Boundary System to support river flow and flood forecasting throughout the United States. Gamma surveys occur in each regional RFC. The gamma flight lines in Figure 2 were flown

222 from September 2015 to April 2018 (black lines). The flight times range from 9 AM to 6 PM
223 according to weather conditions and operations schedule
224 (https://www.nohrsc.noaa.gov/snowsurvey/photos/). The region is dominated by three land cover
225 types, forest (19%, Deciduous broadleaf forest and Mixed forest), croplands (77%, Croplands
226 and Cropland/Natural vegetation mosaic), and grasslands (4%) from Global Mosaics of the
227 Moderate Resolution Image Spectroradiometer (MODIS) land cover type data (MCD12Q1)
228 using the International Geosphere-Biosphere Programme (IGBP) Land Cover Type
229 Classification (Channan et al., 2014). Airborne gamma surveys in the western U.S. were
230 excluded because most of there SM estimates from 2015 to 2018 used a subjective estimate
231 ('SE') or unknown type ('0') (https://www.nohrsc.noaa.gov/snowsurvey).

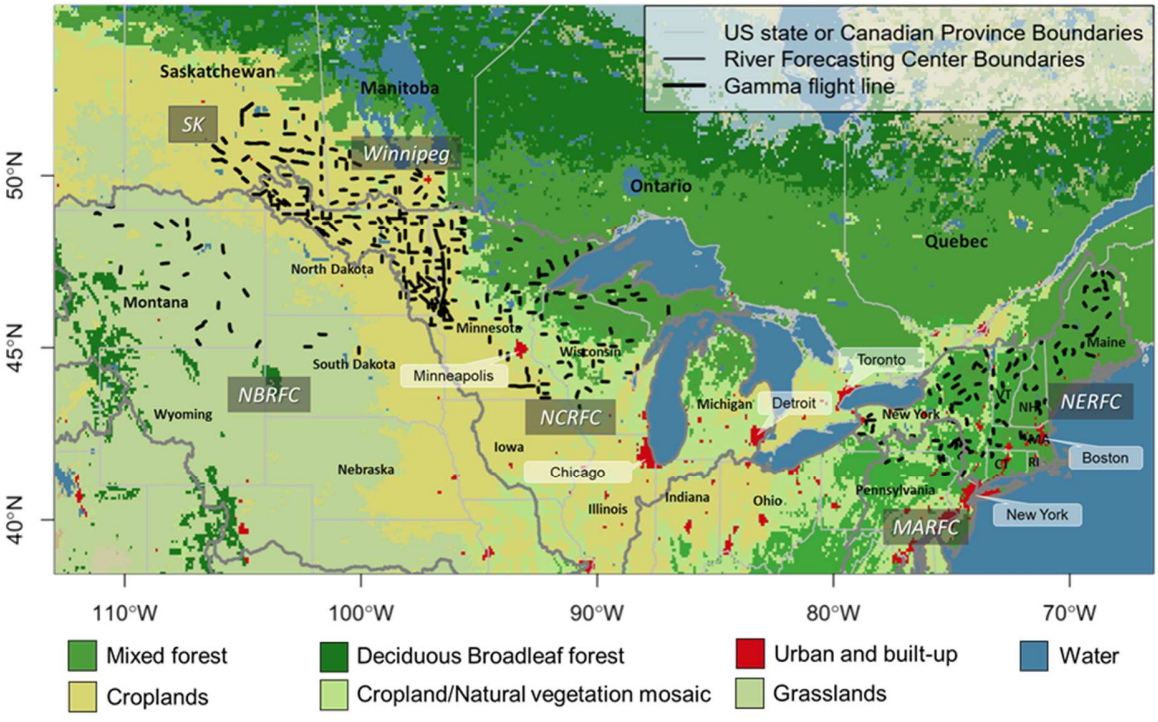

232

Figure 2. Land cover map of the study area of the north-central and eastern United States and southern Canada with the NOAA airborne gamma flight lines surveyed from 2015 to 2018 (N = 574, blue lines with cyan borders) with River Forecasting Center (RFC) boundaries (black lines) along with U.S. states and Canadian province boundaries (gray lines). The land cover map is from Global Mosaics of the Moderate Resolution Image Spectroradiometer (MODIS) land cover type product (MCD12Q1).

4 Data and Methodology

This study uses a number of SM and SWE products (Table 1). The details of each data product appear in the following sections.

Table 1 Summary of soil moisture and snow water equivalent products including data type, period, footprint/grid size, and source used in this study

Data	Product	Type	Period	Footprint/ Grid size	Source
SM & SWE	NOAA gamma	Airborne gamma radiation	2015-2018	5-7 km^2	NOAA
SM	SMAP enhanced	Satellite passive microwave	2015-2017	9 km	NASA
SM	NLDAS-2 Mosaic	Land surface model	2015-2017	12.5 km	NOAA
SM	AMSR2 LPRM	Satellite passive microwave	2015-2017	25 km	NASA
SWE	SSMIS	Satellite passive microwave	2016-2018	25 km	NASA
SWE	GlobSnow	Assimilation	2016-2018	25 km	ESA
SWE	SCAN	In-situ station	2017-2018	point	USDA
SWE	USACE	In-situ field survey	2017-2018	point	USACE

4.1 NOAA Airborne gamma survey

The NWS gamma flight line network includes over 2,400 flight lines covering 29 U.S. states and seven Canadian provinces (Carroll, 2001; Peck et al., 1980). Since 1979, the NWS gamma radiation snow survey program has made about 27,000 gamma SWE measurements over North America via the NOHRSC website (http://www.nohrsc.noaa.gov/snowsurvey/). This study uses the 770 airborne SWE observations made from 2015 to 2018 with 413 flight lines in the study area including 648 observations in non-forested areas. A typical flight line is

approximately 300 m wide and 16 km long (5 km^2 footprint). The gamma survey SM and SWE observations are areal-average values for each flight line footprint, while satellite and model products used in this study are provided as pixel values.

The airborne gamma radiation technique measures the attenuation of the terrestrial gamma radiation signal due to the intervening water mass (Carroll, 2001; Peck et al.,1971). The gamma flux near the ground surface originates primarily from the ^{40}K, ^{208}Tl, and ^{238}U radioisotopes in the soil. In a typical soil, 91% of the gamma radiation signal is emitted from the top 10 cm of the soil and 96% and 99% from the top 20 cm and 30 cm, respectively (Zotimov, 1968). Airborne gamma fall SM measurements can be made for a given flight line if background terrestrial gamma count rates ($^{40}K_0$, $^{208}Tl_0$, and gross count, GC_0) and coincident background SM (SM_0), and gamma count rates are available. Ground-sampled SM data collected over calibration flight lines are used to determine background SM (Jones and Carroll, 1983). Three independent SM values are calculated using the attenuation of the gamma radiation counts. SM values are calculated using gamma count rates from the ^{40}K window (1.36 - 1.56 MeV), ^{208}Tl (2.41 – 2.81 MeV) window, and GC spectrum (0.41 to 3.0 MeV) by the following equations (Carroll, 1981; 2001)

$$SM\left(^{40}K_c\right) = \frac{\frac{^{40}K_0}{^{40}K_C}(100+1.11SM_0)-100}{1.11} \quad \text{Eq. (1)}$$

$$SM\left(^{208}Tl_c\right) = \frac{\frac{^{208}Tl_0}{^{208}Tl_C}(100+1.11SM_0)-100}{1.11} \quad \text{Eq. (2)}$$

$$SM(GC_c) = \frac{\frac{GC_0}{GC_c}(100+1.11SM_0)-100}{1.11} \quad \text{Eq. (3)}$$

$$SM_c = 0.346 \cdot SM\left(^{40}K_c\right) + 0.518 \cdot SM\left(^{208}Tl_c\right) + 0.136 \cdot SM(GC_c) \quad \text{Eq. (4)}$$

where $^{40}K_c$, $^{208}Tl_c$, and GC_c are current uncollided gamma count rates in windows ^{40}K, ^{208}Tl, and GC, respectively, and $^{40}K_0$, $^{208}Tl_0$, and GC_0 are background uncollided gamma count rates. A single current SM estimate (SM_c, in units of percent by weight) is calculated by multiplying the three current SM estimates by weighting factors, 0.346, 0.518, and 0.136 for ^{40}K, ^{208}Tl, and GC, respectively (Jones & Carroll, 1983). Only the single, weighted SM (SM_c) is reported as antecedent fall SM which is used in this study. The fall SM survey data are available as Standard Hydrometeorological Exchange Format (SHEF) product through the NWS NOHRSC website (https://www.nohrsc.noaa.gov/snowsurvey/).

The operational gamma SWE measurements are made using the following equations:

$$SWE\left(^{40}K\right) = \frac{1}{A} \cdot \left[ln\left(\frac{^{40}K_b}{^{40}K_s}\right) - ln\left(\frac{100+1.11 \cdot SM\left(^{40}K_s\right)}{100+1.11 \cdot SM\left(^{40}K_b\right)}\right)\right] \quad \text{Eq. (5)}$$

$$SWE\left(^{208}Tl\right) = \frac{1}{A} \cdot \left[ln\left(\frac{^{208}Tl_b}{^{208}Tl_s}\right) - ln\left(\frac{100+1.11 \cdot SM\left(^{208}Tl_s\right)}{100+1.11 \cdot SM\left(^{208}Tl_b\right)}\right)\right] \quad \text{Eq. (6)}$$

$$SWE(GC) = \frac{1}{A} \cdot \left[ln\left(\frac{GC_b}{GC_s}\right) - ln\left(\frac{100+1.11 \cdot SM(GC_s)}{100+1.11 \cdot SM(GC_b)}\right)\right] \quad \text{Eq. (7)}$$

$$SWE_{gam_{oper}} = 0.346 \cdot SWE\left(^{40}K\right) + 0.518 \cdot SWE\left(^{208}Tl\right) + 0.136 \cdot SWE(GC) \quad \text{Eq. (8)}$$

where $SM\left(^{40}K_b\right)$, $SM\left(^{208}Tl_b\right)$, and $SM(GC_b)$ are SM values by weight (%) over bare ground and $SM\left(^{40}K_s\right)$, $SM\left(^{208}Tl_s\right)$, and $SM(GC_s)$ are SM values over snow-cover ground. $^{40}K_b$, $^{208}Tl_b$, and GC_b are uncollided gamma count rates over bare ground and $^{40}K_s$, $^{208}Tl_s$, and GC_s for snow-covered ground. $SWE_{gam_{oper}}$ is the operational gamma radiation SWE estimate (g/cm^2) reported in the SHEF product (Carroll and Schaake Jr, 1983; Carroll, 2001). Based on previous studies, errors of the airborne gamma SM measurement range from - 9.9 to 2.9% of percent bias (Carroll, 1981). Errors of the gamma SWE were about 12.1% over agricultural areas in the Upper

Midwest U.S. and 1.3 – 24% over forested areas of the Lake Superior basin, U.S. and Saint John River basin, Canada. (Carroll and Carroll, 1989a; Carroll, 2001; Glynn et al., 1988). Glynn et al. (1988) indicate that the potential sources of errors in gamma SWE estimates include gamma count statistics, navigation, and biomass.

The airborne gamma SM estimate is provided as "percent SM by weight" which is the weight of SM divided by the weight of dry soil multiplied by 100 from approximately the top 20 cm of soil. To compare the gamma SM (by weight, %) to the gridded SM products (volumetric content, m^3/m^3), the units of SM were matched. The percent airborne gamma SM by weight was converted to volumetric SM contents (m^3/m^3) using the constant bulk density (1.295 g/cm^3) based on a dominant soil bulk density in this study area (Dobson et al., 1985). Our results show that using a constant bulk density as compared to individual bulk density for each gamma footprint using the 1-km POLARIS soil datasets (available at www.polaris.earth; Chaney et al., 2016) does not generate additional residual errors in the comparison between gamma SM and other SM products (Figure S1 & S2).

4.2 Soil moisture (SM)

4.2.1 SMAP enhanced SM

The NASA's SMAP satellite's L-band radiometer has provided global SM measurements at 6:00 A.M./P.M. local time at 2–3 days revisit time since March 31, 2015 (Chan et al., 2016; Entekhabi et al., 2010). The SMAP SM product has been validated using ground-based observations and various assimilation products at a global scale (Kim et al., 2018; Colliander et al., 2017; Ma et al., 2019; Zhang et al., 2019; Zwieback et al., 2018).

313 The SMAP enhanced L3 SM, released in December 2016, is derived from SMAP Level-
314 1C (L1C) interpolated brightness temperatures using Backus-Gilbert optimal interpolation
315 techniques (O'Neill et al., 2018). The SMAP enhanced SM product (9 x 9 km^2) retrieved by the
316 SCA (V-pol) has a finer grid posting relative to the SMAP native products (36 x 36 km^2)
317 although the enhanced footprint's contributing domain is ~ 33km is similar to the native 36 km
318 resolution (Chan et al., 2018). In this study, the SMAP level 3 radiometer global daily EASE-
319 Grid 2.0 (Equal-Area Scalable Earth Grid 2.0) enhanced soil moisture (V002) for the
320 descending overpass (6 A.M.) is used from September 2015 to March 2018. This product (V002)
321 has an improved depth correction for effective soil temperature, which reduced the dry bias in
322 the initial version product (V001) (O'Neill et al., 2018).

323 **4.2.2 AMSR2 SM**

324 The AMSR2 passive microwave sensor, a follow-on of the AMSR-E sensor aboard the
325 Aqua satellite, was launched on the GCOM-W1 satellite in May 2012 (Imaoka et al., 2010). The
326 AMSR2 provides daily scans at 1:30 A.M. (descending) / P.M. (ascending) local time with 1–2
327 days revisit time. There are three widely used AMSR2 surface SM products generated from
328 different algorithms, the LPRM (Land Parameter Retrieval Model) (Owe et al., 2008), the JAXA
329 algorithm (Koike, 2013; Cho et al., 2015) and the SCA (Single Channel Algorithm; Bindlish et
330 al., 2018). The LPRM uses the dual-polarization Tb observations at individual (C or X) bands to
331 retrieve surface SM and vegetation optical depth via a forward radiative transfer model (Owe et
332 al., 2008). This study uses the LPRM AMSR2, Level 3 gridded X-band (10.7 GHz) SM from the
333 ascending overpass, expressed on a regular 1/4° spatial grid (25 km).

334 **4.2.3 NLDAS-2 Mosaic SM**

The NLDAS-2 is an offline modeling system, running four land surface models [Noah, Mosaic, Sacramento soil moisture accounting (SAC), and the Variable Infiltration Capacity (VIC) model] on a 1/8° spatial grid (12.5 km) over the continental United States (CONUS). NLDAS-2 uses meteorological forcing data (e.g. downward short/longwave radiation, precipitation, 2-m air temperature, 2-m specific humidity, and 10-m wind speed) to run the land surface models to produce water and energy fluxes and state variables (Xia et al., 2012). The NLDAS-2 has SM products from four land surface models (Mosaic, Noah, SAC, and VIC) (Xia et al., 2014). The Mosaic model has three soil layers: 0–10 cm, 10–60 cm, and 60–200 cm (Koster & Suarez, 1996). In this study, the Mosaic 12:00 PM SM at a depth of 0-10 cm is used to represent modeled SM values, because the Mosaic SM had a stronger agreement with the airborne gamma SM than the Noah and VIC SM products from the surface soil layer [0-10 cm] (Figure S3). The SAC SM was not compared because it uses a single soil layer with no surface soil moisture.

In summary, this study uses SMAP and AMSR2 SM products as well as the NLDAS-2 Mosaic SM product. Active microwave satellite (e.g. ASCAT) SM is not included because recent studies found that passive microwave SM (e.g. SMAP/SMOS) products generally have a stronger agreement with in-situ observations or reanalysis SM products than ASCAT SM over our study region (Al-Yaari et al., 2014; Kim et al., 2018).

4.3 Snow water equivalent (SWE)

4.3.1 SSMIS SWE

The SSMIS sensor onboard the Defense Meteorological Satellite Program (DMSP) F17 platform has provided daily brightness temperature (Tb) measurements with near-complete

global coverage from December 2006 to the present. In this study, F17 SSMIS SWE (SWE_{SSMIS}) was estimated using the Chang-type algorithm (Armstrong and Brodzik, 2001; Chang et al., 1987) with modified coefficients developed by Brodzik (2014) as follows:

$$SWE_{SSMIS} = a \cdot Tb_{H,19GHz} - b \cdot Tb_{H,37GHz} - c \quad \text{Eq. (9)}$$

where *a, b,* and *c* are given as 4.807 mm/K, 4.792 mm/K, and 6.036 mm, respectively. $Tb_{H,19GHz}$ and $Tb_{H,37GHz}$ are the brightness temperature at 19 and 37 GHz horizontal polarization, respectively. The DMSP SSM/I-SSMIS Pathfinder Daily EASE-Grid Brightness Temperatures (Version 2) are provided on a 25-km grid on the National Snow & Ice Data Center website (https://nsidc.org/data/nsidc-0032; Armstrong et al., 1994). SSMIS Tb data from the descending overpass (6 A.M.) were used to minimize the potential error by wet snow (Derksen et al., 2000).

4.3.2 GlobSnow SWE

The European Space Agency GlobSnow project provides long-term gridded daily SWE maps with 25 km x 25 km spatial resolution from 1979 to current for the Northern Hemisphere, except for glaciers and mountainous regions (Takala et al., 2011). The GlobSnow SWE utilizes an assimilation approach, which combines ground-based synoptic snow depth station data (using constant snow density, 0.24 kg/m^2) with passive microwave satellite measurements via the Helsinki University of Technology (HUT) snow emission model (Takala et al., 2011; Pulliainen, 2006). Ground-based point snow depth measurements are from the World Meteorological Organization weather stations. The GlobSnow SWE has two versions, GlobSnow-2 from 1979 to 2016 (archive_v2.0; http://www.globsnow.info/swe/archive_v2.0/) and GlobSnow-1 from 2011 to current (near-real-time; http://www.globsnow.info/swe/nrt/). The retrieval accuracy is the same between the GlobSnow-1 and 2, but the GlobSnow-2 SWE was improved for northern

boreal forest and tundra regions (Luojus et al., 2014). Due to the current study period from 2015 to 2018, the daily GlobSnow-1 SWE was used to evaluate the updated gamma SWE.

4.3.3 Ground-based SWE

Compared to the western U.S., there are few SWE stations in the north-central and northeastern U.S. Daily SWE measurements at the Glacial Ridge, Minnesota (ID: 2050; Latitude/Longitude: 47.72°/96.26°; Elevation: 343 m) operated by the United States Department of Agriculture (USDA) Soil Climate Analysis Network (SCAN) were compared to the updated gamma SWE measurements. The SCAN site land cover is "croplands" with a "prairie" snow classification. Two gamma flight lines, MN119 and MN120, are located near the SCAN site with the flight lines' midpoints approximately 9.8 km (northwards) and 29.7 km (southwards), respectively, from the SCAN site. The two flight lines' land cover is also "cropland" and their elevations are about the same (Figure S4). Further details can be found on the SCAN website (https://wcc.sc.egov.usda.gov/nwcc/site?sitenum=2050).

The United States Army Corps of Engineer (USACE) ground-based snow survey data were collected by the USACE St. Paul District to determine snowpack SWE for spring flood risk assessment and water resources management. Their survey measurements sampled the snowpack at representative locations. At each site and date, at least four SWE samples were taken, each approximately 3–4 m apart, using a snow tube (3.81 cm diameter), then averaged to a single mean SWE value. This study uses the weekly USACE SWE observations from 2017 to 2018 at Baldhill, ND (Latitude/Longitude: 47.03°/-98.08°), Orwell, MN (46.22°/-96.18°), and Traverse, MN (45.86°/-96.57°). The gamma flight lines closest to each site with a distance between the midpoint of flight line and the site are ND432 and ND433 (10.6 km and 26.3 km from Baldhill), MN126 and MN129 (24.8 km and 19.2 km from Orwell), and ND441 and MN124 (13.8 km and

22.6 km from Orwell). The detailed gamma flight line locations are provided in Supplementary material (Figure S4).

4.4 Methodology

For comparison to the airborne gamma SWE data, the satellite or model pixels overlapped by the given flight line footprint were weighted according to a portion of the footprint within each pixel. Only flight lines having more than 50% of the footprint covered by satellite observations were used in this analysis. For a detailed process with a schematic diagram, please refer to Tuttle et al. (2018).

After one SM product (in this case, the SMAP enhanced SM) was selected based on the statistical agreement (e.g. correlation coefficient and unbiased root mean square difference) with operational baseline gamma SM, a linear regression model that minimizes the sum of squared residuals (ε_i) was developed to relate coincident gamma SM ($SM_{gam,i}$) and the satellite (or model) SM ($SM_{sat,i}$) measurements.

$$SM_{gam,i} = a \cdot SM_{sat,i} + b \pm \varepsilon_i \quad \text{Eq. (10)}$$

where *i* is flight line number, *a* is the slope and *b* is the y-intercept of the linear regression equation. ε_i is a residual error (m^3/m^3) between operational gamma SM and satellite (or model) SM for each flight line. Based on the model, new, updated gamma SM estimates were calculated by applying the latest antecedent SM of the chosen product into the linear regression model. It is assumed that the residual, ε_i, is largely generated from differences between the two products' representative areas and land surface characteristics for each flight line. Thus, the residuals are included in the updated gamma SM.

The change in airborne gamma SWE, $\Delta SWE_{gam,i}$, resulting from a change in antecedent SM in the unit of percentage (%) in soil was calculated using Carroll (2001) as follows:

$$\Delta SWE_{gam,i} = \frac{25.4}{A} \cdot \left[\ln \left(\frac{100+1.11 \cdot SM_{gam_{oper},i}}{100+1.11 \cdot SM_{gam_{upd},i}} \right) \right] \quad \text{Eq. (11)}$$

where $\Delta SWE_{gam,i}$ is the change in snow water equivalent (mm), A is a radiation attenuation coefficient of water which is equal to 0.1482 (Carroll, 2001). 25.4 is used to convert "inches" to "mm" from Equation 3 in Carroll (2001). 1.11 represents the ratio of gamma radiation attenuation in water to air (Carroll, 1981). $SM_{gam_{oper},i}$ is operational gamma SM by weight (%) measured in the fall survey and $SM_{gam_{upd},i}$ is the updated gamma SM by weight (%). A schematic diagram of the methodology is provided in the Supplementary materials (Figure S5). The agreement between airborne gamma survey and satellite/model SM (or SWE) products was quantified by the Pearson's linear correlation coefficient, *R*, the mean bias, *Bias*, the root mean square difference, *RMSD*, and the unbiased RMSD, *ubRMSD*. The equations are available in the Supplementary material (Text S1).

5 Results

5.1 Change in the soil moisture after baseline gamma flights from satellite and model products

Figure 3 compares the change in NLDAS-2, SMAP, and AMSR2 regional SM maps from the dates of the baseline fall gamma flights until the last observation before freeze onset. As an example, in 2016 most gamma SM flights occurred about 25 October and the latest observation available prior to freezing onset was on 29 November. After the fall gamma flights, SM changes vary by year and location. These changes are typically caused by later rainfall, early-winter

444 snowmelt, and/or freeze/thaw events, suggesting that an adjustment of the baseline gamma SM is
445 necessary for accurate gamma SWE survey.

446 In 2015, the change in NLDAS-2 and SMAP SM from November 25 to December 12
447 show similar spatial patterns. Surface soils became wetter in the north-central U.S. and drier in
448 the northeastern U.S. The increases in SMAP SM are greater than NLDAS in Minnesota, North
449 Dakota, and South Dakota where many of the gamma flights occurred. The AMSR2 SM change
450 is remarkably different from NLDAS-2 and SMAP SM. AMSR2 shows drying in Minnesota and
451 most Canadian provinces. In 2016, SM changes clearly differ by data source between 25 October
452 and 29 November. SMAP has a strong drying signal of up to -0.17 m^3/m^3 in north-central and
453 eastern U.S. as well as Saskatchewan and Manitoba, Canada. However, NLDAS-2 and AMSR2
454 SM in the same regions get wetter by up to 0.12 and 0.25 m^3/m^3, respectively. In the Midwest,
455 AMSR2 shows that SM increases exceed 0.25 m^3/m^3. In 2017, there are clear decreases in
456 NLDAS-2 and SMAP SM from 25 October to 13 December in the Midwest. The drying of
457 SMAP (~0.20 m^3/m^3) is stronger than that of NLDAS-2 (~0.10 m^3/m^3). NLDAS-2 captures
458 modest wetting in Canada, which is not seen by SMAP and AMSR2 SM because these datasets
459 are provided for only limited areas in Canada, due to data masking from soil freeze or snow
460 cover.

461 In general, SMAP SM changes are spatially similar to NLDAS-2 SM changes but have
462 amplified drying (and wetting). AMSR2 has extreme SM changes considering the normal range
463 of volumetric SM and differs spatially from SMAP and NLDAS-2, which may reflect the much
464 thinner and closer-to-the-surface sensing depth of AMSR2 as compared to SMAP and NLDAS-
465 2's deeper sensing depths.

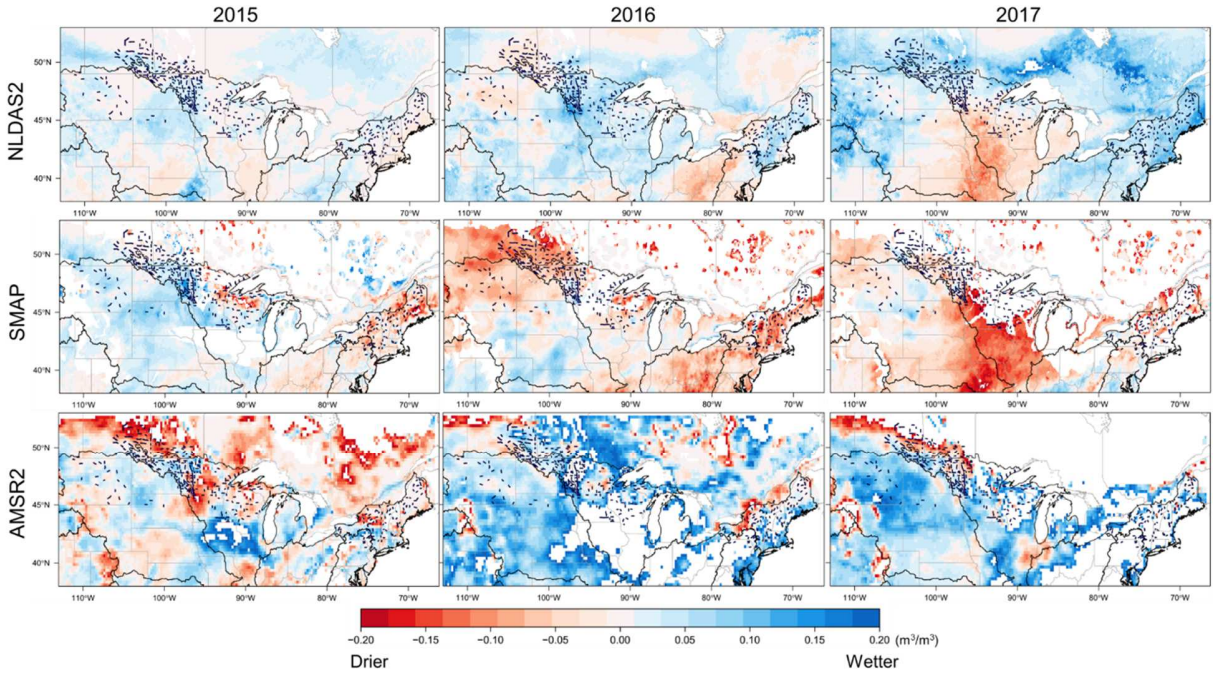

Figure 3. **SM difference maps for NLDAS-2, SMAP, and AMSR2 for the years 2015 to 2017.** SM differences are calculated between the date of the fall baseline gamma flights and the date of the last SM observation prior to freezing onset. A past 5-day composite SM map was used to eliminate spatial gaps.

5.2 Airborne gamma SM versus satellite and model SM products

To identify which satellite or model SM product agrees best with gamma SM, the gamma SM data were compared to NLDAS-2, SMAP, and AMSR2 SM products. Because the performance of the microwave SM products typically weakens with increasing vegetation density (Jackson & Schmugge, 1991; Wang et al., 1982; Mladenova et al., 2014), the comparison is conducted with and without forest areas. When forested areas are included, NLDAS-2 SM has better agreement with operational gamma SM than the two satellite SM products (Table 1). There is little difference in agreement between NLDAS-2 mosaic SM and operational gamma SM with/without forest classes (Figure 4a & b). However, the agreement between SMAP and gamma SM clearly differs by a land cover (Figure 4c & d). A majority of the SMAP SM values

with a wet bias occur for flights over forests. For the Deciduous broadleaf forest and Mixed forest classes, there are large errors with SMAP SM compared to gamma SM (*Bias*: 0.11 and 0.19 m^3/m^3 and *RMSD:* 0.17 and 0.21 m^3/m^3, respectively). For the AMSR2 comparison, most SM values over forested areas were excluded due to poor data quality before the analysis, but the remaining SM values show a wet bias, similar to SMAP SM, in forested regions (Figure 4e). AMSR2 SM has an extreme wet bias (0.13 m^3/m^3) even in non-forested areas. In non-forested regions, SMAP SM shows very strong agreement with gamma SM as compared to AMSR2 and NLDAS-2 SM (Table 2). The results indicate that SMAP SM values from forested areas (e.g. Deciduous broadleaf forest and Mixed forest) do not agree with the gamma observations and these land uses should be excluded if updating gamma SWE with SMAP SM. A linear regression model between SMAP and operational gamma SM [Eq. (10)] was developed using only the values from non-forested regions for the next step. Comparison between operational gamma SM and SMAP, AMSR2, and NLDAS-2 SM products for forested regions only, are provided in Figure S6.

Table 2 Agreement between NOAA airborne gamma SM and NLDAS-2 Mosaic SM, SMAP enhanced SM, and AMSR2 SM with/without the SM values from forested areas

Data	with forested areas					without forested areas				
	N	*R*	*ubRMSD* (m^3/m^3)	*RMSD* (m^3/m^3)	*Bias* (m^3/m^3)	N	*R*	*ubRMSD* (m^3/m^3)	*RMSD* (m^3/m^3)	*Bias* (m^3/m^3)
NLDAS-2	342	0.53	0.07	0.08	-0.03	277	0.53	0.07	0.08	-0.03
SMAP	342	0.52	0.10	0.10	0.02	277	0.69	0.06	0.06	-0.02
AMSR2	287	0.43	0.08	0.15	0.13	278	0.45	0.07	0.15	0.13

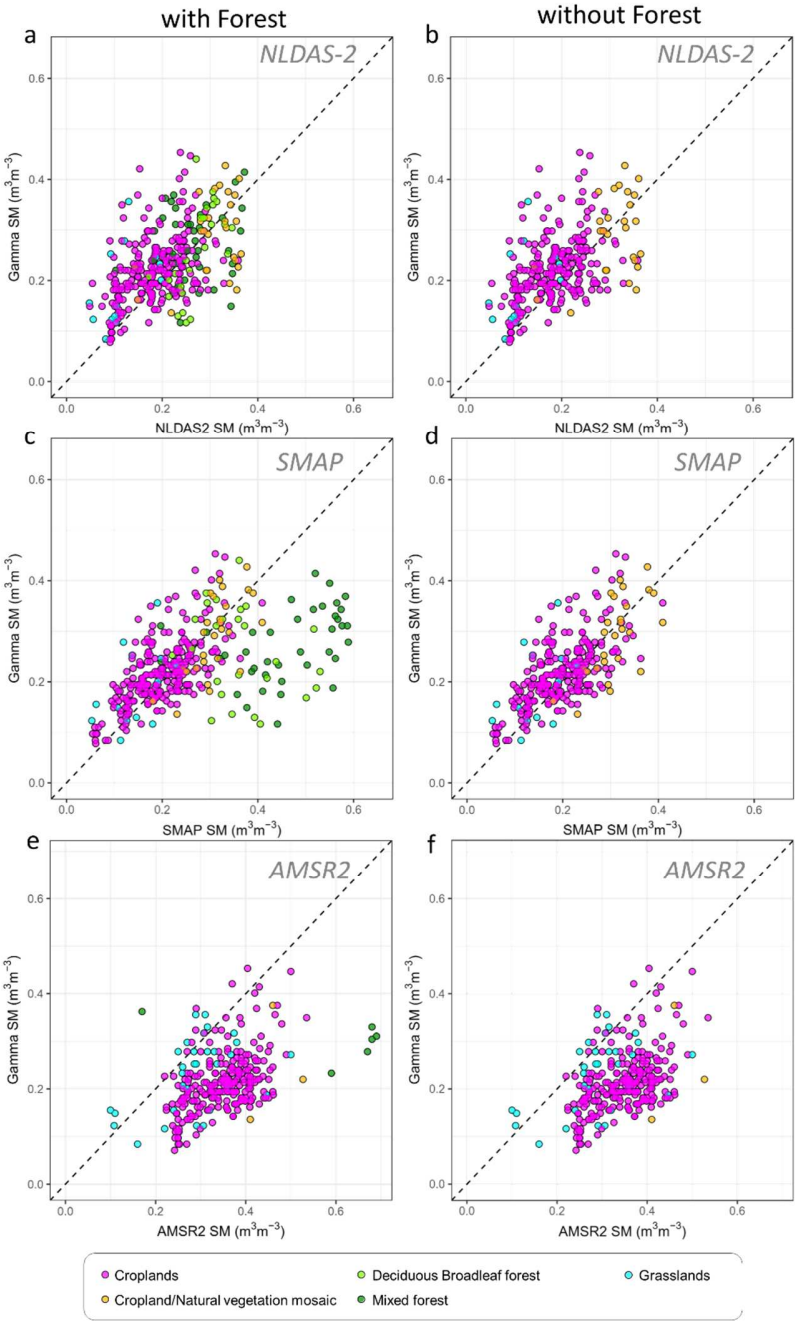

498

499 **Figure 4**. Comparison of NOAA airborne gamma soil moisture with (a, b) Phase 2 of the North
500 American Land Data Assimilation System (NLDAS-2) Mosaic SM, (c, d) Soil Moisture Active
501 Passive (SMAP) Level 3 enhanced soil moisture, and (e, f) Advanced Microwave Scanning
502 Radiometer 2 (AMSR2) SM within the given flight line footprints with/without the SM values
503 from forested areas.

504

5.3 Enhancement of gamma SWE by updating baseline SM

When the operational, baseline gamma SM in non-forested regions from 2015 to 2017 are updated using SMAP SM, the gamma SWE values change. Figure 5a displays SMAP SM changes measured between the date of the fall baseline gamma flights and the date of the last SM observation before freeze-up as well as the corresponding operational and SMAP-updated airborne gamma SM estimates. The SMAP-updated gamma SM were calculated using the linear regression model between airborne gamma and SMAP SM, slope (a) = 0.69 and y-intercept (b) = 0.083 [Eq. (10)]. The slope indicates that SMAP SM is more sensitive than gamma SM. Considering the two methods' different representative soil depths, it is reasonable that SMAP's surface SM would tend to have higher variability than the deeper gamma SM.

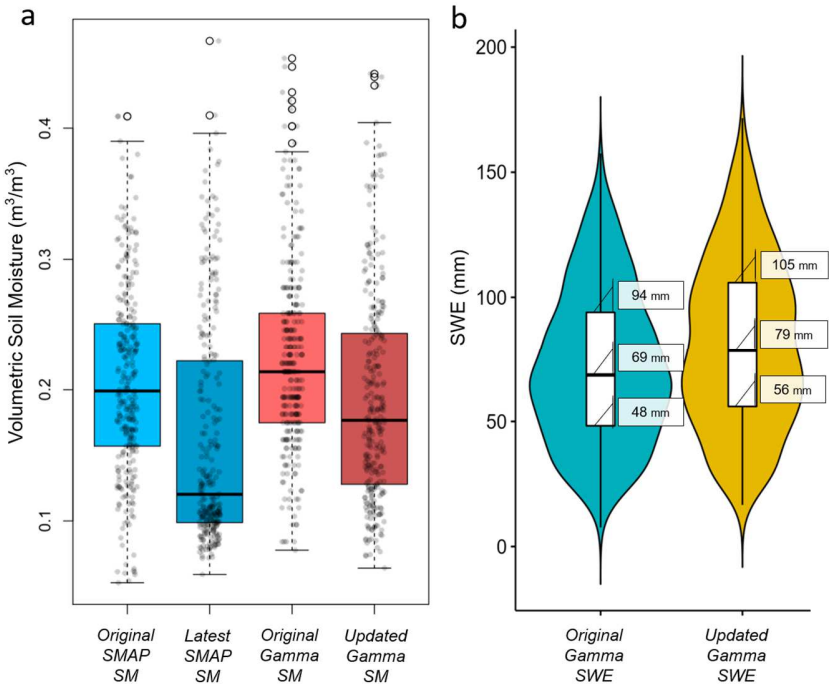

Figure 5. (a) Boxplots of SMAP SM at original (operational) and latest available dates and original and updated gamma SM for entire flight lines in the non-forested region from 2015 to 2017, along with (b) the corresponding original and updated gamma SWE. (a) The small circles are individual SM data (no meaning for a spread in the horizontal direction) and the larger circles are outliers. The bold line within each colored box is median, and the upper and bottom sides of the box are the upper (75%) and lower (25%) quantiles of the data. (b) The width of the leaf-shape boxplot shows the relative amount of the SWE data at that magnitude.

523

524 The SMAP SM immediately before freeze-up (mean: 0.16 m^3/m^3, median: 0.12 m^3/m^3) is
525 typically lower than the SM on the date of the fall baseline gamma flights (mean: 0.21 m^3/m^3,
526 median: 0.20 m^3/m^3), indicating that for this study period most of the region dried in late fall to
527 early winter. Note: a large portion of the gamma SM flights (193 of total 277 flight lines)
528 occurred in fall 2016 when there was an average of 0.05 m^3/m^3 (median: 0.09 m^3/m^3) decrease in
529 SMAP SM. As the SMAP SM differences between the baseline and latest available SM decrease,
530 the gamma SM differences should also decrease following the linear regression model [Eq. (10)].
531 The SMAP-updated gamma SM is drier by an average of 0.03 m^3/m^3 than the operational
532 baseline gamma SM. The SMAP-updated gamma SM also appears to have a greater interquartile
533 range (IQR; total: 0.12 m^3/m^3) than the operational baseline gamma SM (0.08 m^3/m^3). This
534 indicates that the residual values (ε_i) in the linear regression model comprise a considerable
535 proportion of the variation in SMAP-updated gamma SM.

536 Using the SMAP-updated SM for each flight footprint, a new, SMAP-updated gamma
537 SWE was calculated using Eq. (10). The original, operational gamma SWE values (mean: 72
538 mm, median: 69 mm) were adjusted upward by 15% (mean: 82 mm, median: 79 mm) when
539 accounting for the changes in baseline SM (Figure 5b). In summary, decreases in the baseline
540 SM by an average of 0.03 m^3/m^3 (gamma) and 0.05 m^3/m^3 (SMAP) generate average increases in
541 gamma SWE of about 10 mm. Individual gamma SWE estimates have different SM changes due
542 to the variations by year and flight line as presented in Figure 6. 75% of the SM values became
543 drier and the remaining 25% became wetter, but with SM differences ranging from 0.22 to -0.25
544 m^3/m^3 and gamma SWE changes ranging from -30 to 41 mm.

545

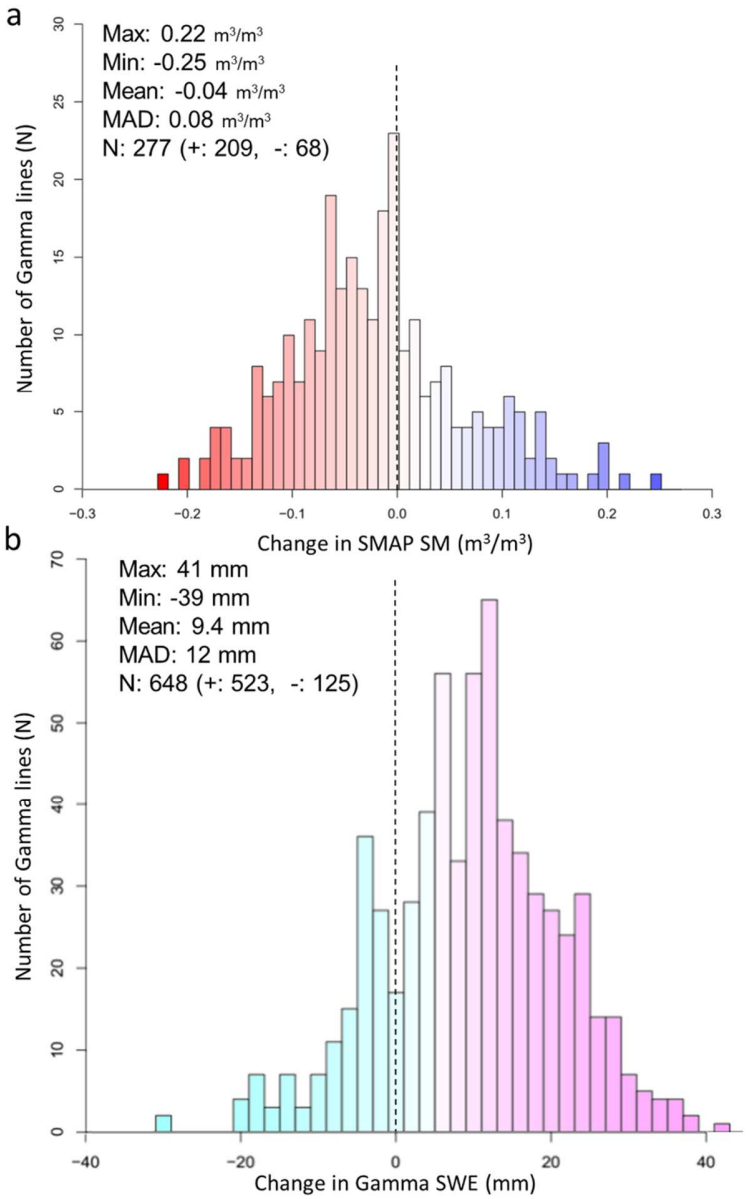

546 **Figure 6**. Histogram of (a) changes in SMAP SM and (b) NOAA airborne gamma SWE from the
547 date of the baseline fall gamma flights to the date immediately before winter freeze-up
548

549 **5.4 Evaluation of the updated gamma SWE**

550 To evaluate the SMAP-updated gamma SWE, satellite-based SWE measurements from
551 SSMIS passive microwave sensors were used. Flight lines in forest-dominant regions were

552 excluded because SSMIS underestimates SWE compared to airborne gamma SWE over the
553 forested areas (Figure S7). Figure 7 shows that the SSMIS SWE has better agreement with
554 SMAP-updated gamma SWE than with the operational gamma SWE. When the SSMIS SWE
555 exceeds 125 mm, the SMAP-updated gamma SWE values with high DOY converge toward the
556 1:1 line. The agreement between the two SWE estimates was improved for each land cover type
557 when gamma SWE was updated with SMAP SM (Figure S8). In grassland, the SSMIS SWE had
558 a higher correlation and lower *ubRMSD* with SMAP-updated gamma SWE as compared to the
559 agreement with the operational SWE. There were also modest improvements in the agreement
560 statistics in croplands, except for *Bias*, which increases from -1.8 to -11 mm.

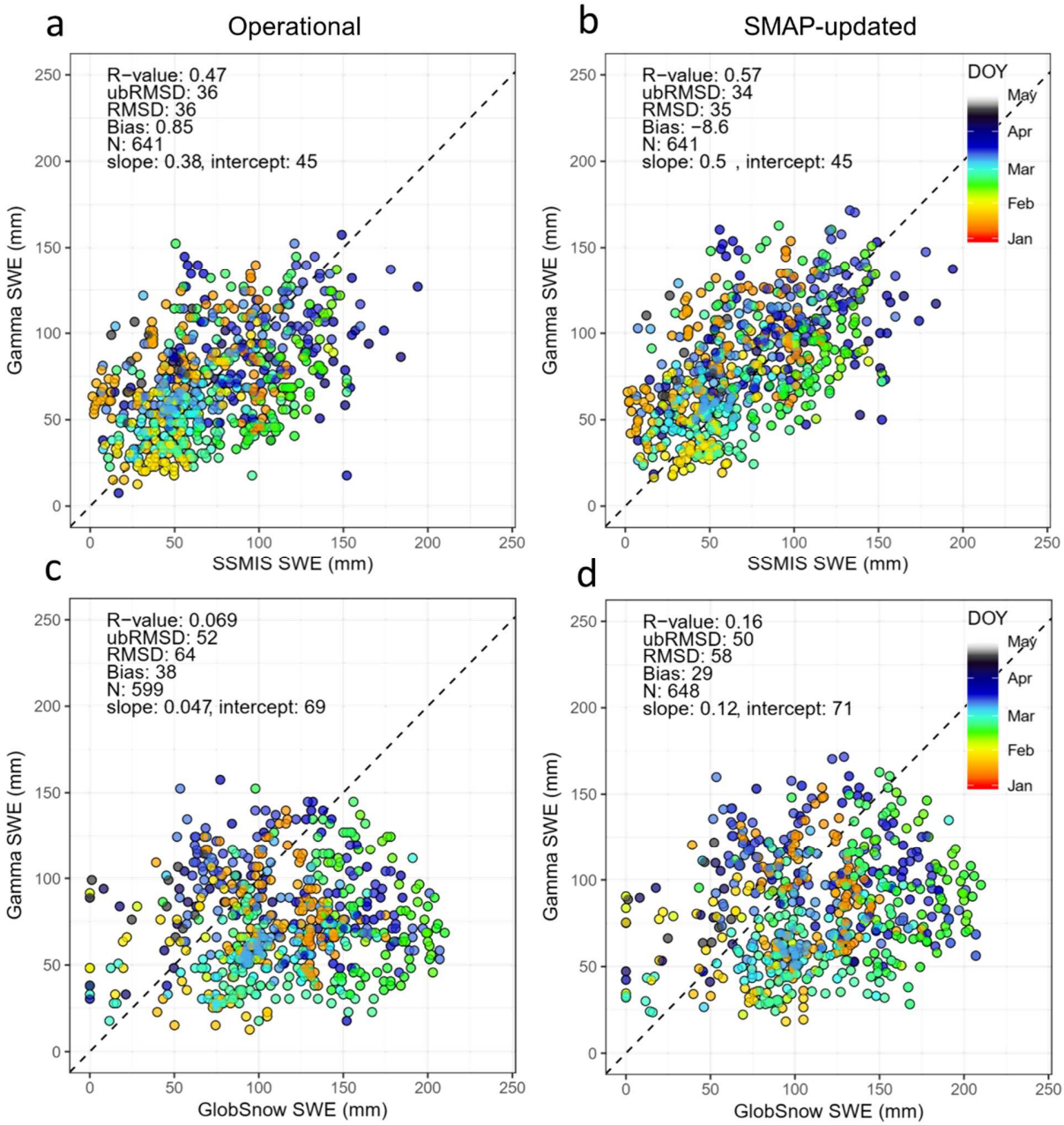

Figure 7. Comparison between operational and SMAP-updated NOAA airborne gamma snow water equivalent with (a, b) satellite-based snow water equivalent from Special Sensor Microwave Imager Sounder (SSMIS) and (c, d) ESA GlobSnow assimilation SWE within the given flight line footprint. The points are colored by day of year (DOY).

To further validate the SMAP-updated gamma SWE, ground-based SWE measurements were obtained from the Glacial Ridge SCAN site snow pillow. Even though there are only five coincident gamma SWE observations, the gamma SWE captures the SWE evolution of the in-

situ data for the two years (Figure 8). In 2017, gamma SWE updates were only 3 mm because of the limited changes in the baseline SM. In 2018, the operational gamma SWE values are updated by about 20 mm due to the large decrease in the antecedent SM. The updated gamma SWE shows a higher correlation ($R = 0.95$ with $p < 0.01$) with in-situ SWE than the operational gamma SWE ($R = 0.75$ with $p = 0.15$; Figure 8b). The slope and y-intercept of the updated SWE are also much closer to the 1:1 line. While the operational gamma SWE overestimated SWE by 8 mm in 2017, it underestimated SWE by 12 mm in 2018. The updated gamma SWE biases are consistent for both years.

A final comparison was conducted using the weekly SWE samples from the United States Army Corps of Engineer (USACE) at three sites (Baldhill, ND, Orwell, MN, and Traverse, MN) in the north-central U.S. (see Figure S4). The USACE SWE shows better agreement with the SMAP-updated SWE ($R = 0.71$ with $p = 0.075$) than the operational gamma SWE ($R = 0.65$ with $p = 0.12$; Figure 9).

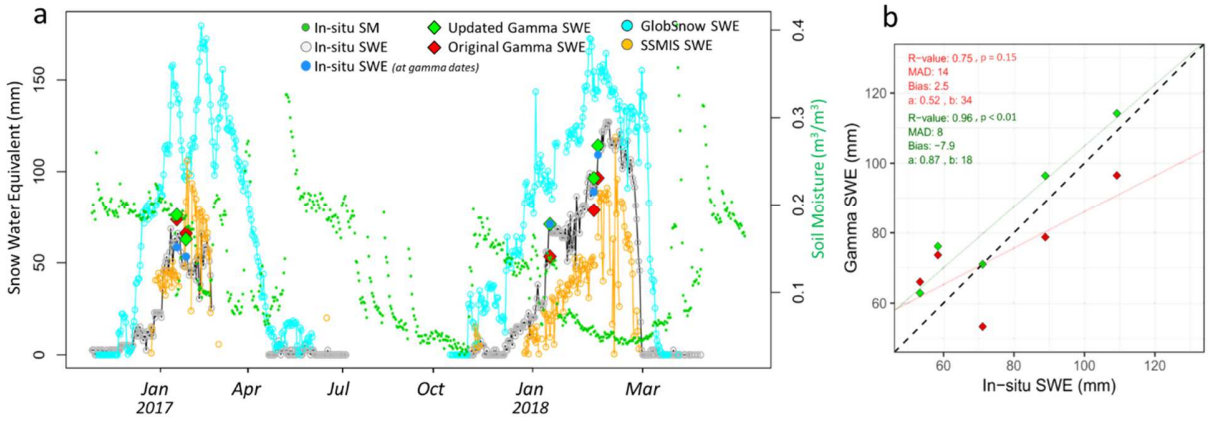

Figure 8. (a) Time series of in-situ SM and SWE measurements with the operational and SMAP-updated gamma SWE at the Glacial Ridge Station, Minnesota (ID: 2050) from the Soil Climate Analysis Network (SCAN) and (b) agreement between the in-situ SWE and the operational and SMAP-updated gamma SWE. The red points in both plots indicate the operational gamma SWE, while the green points indicate SMAP-updated gamma SWE.

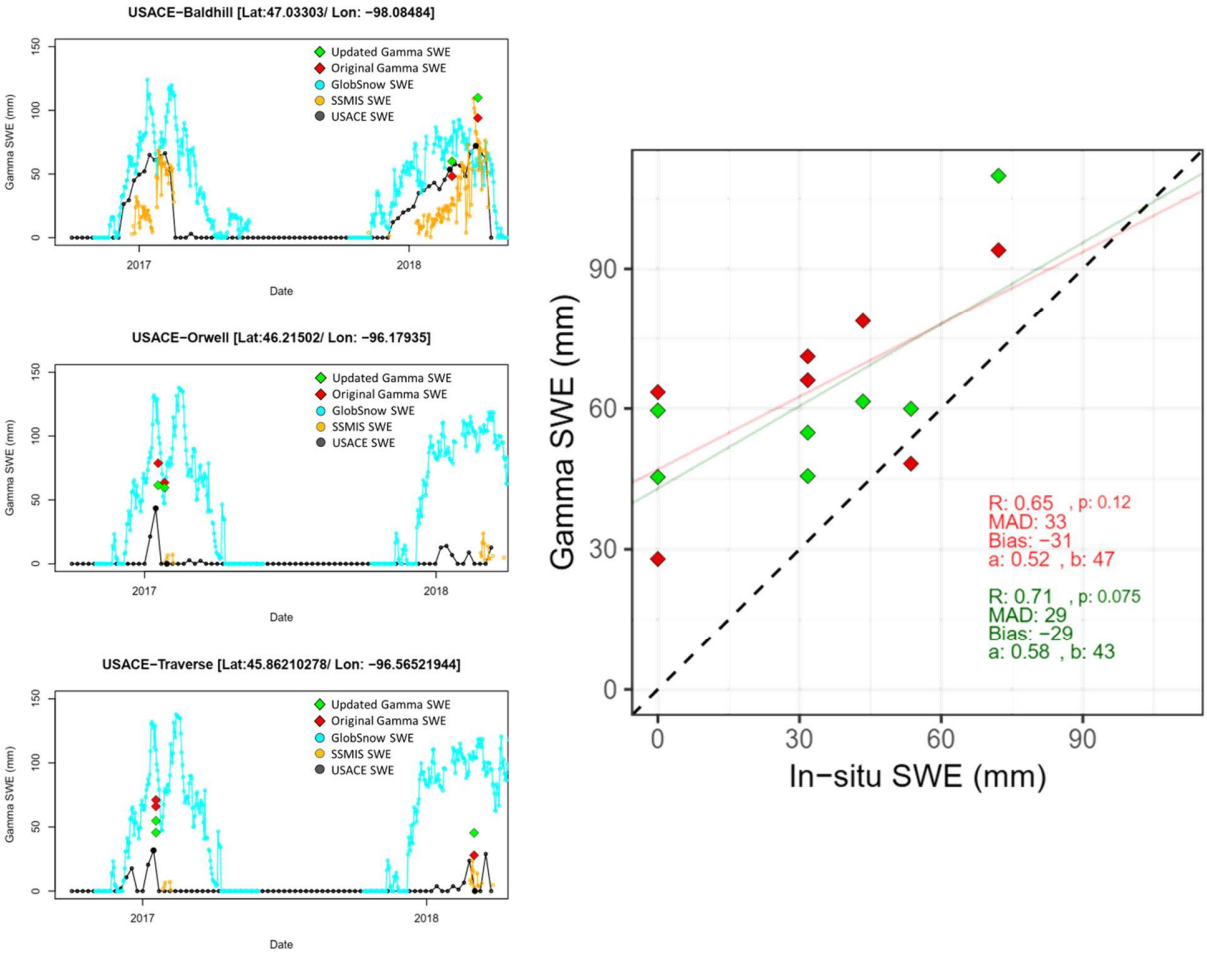

Figure 9. (a) Time series of in-situ SWE measurements with the operational and SMAP-updated gamma SWE at three sites (Baldhill, ND, Orwell, MN, and Traverse, MN) from the United States Army Corps of Engineers (USACE) and (b) agreement between the in-situ USACE SWE and the operational and SMAP-updated gamma SWE. The red points in both plots indicate the operational gamma SWE, while the green points indicate SMAP-updated gamma SWE.

6 Discussion

6.1 Evaluation of soil moisture

The superior agreement of SMAP products with gamma SM in non-forested areas could be caused by its finer spatial resolution (9 km x 9 km) as compared to AMSR2 (25 km x 25 km) and NLDAS-2 (12.5 km x 12.5 km). Considering that the typical gamma flight line has a 5–7 km^2 footprint, the finer resolution of the SMAP enhanced SM may lead to less spatial

heterogeneity error within the pixels (Loew, 2008; Chan et al., 2018). However, Cho et al. (2018) found that the gamma SM also had better agreement with SMAP standard SM (36 km x 36 km; SPL3SMP) than with either the AMSR2 or the NLDAS-2 mosaic SM products. This result is similar to Kim et al.'s (2018) finding that in-situ SM showed better agreement with the SMAP standard SM than with either AMSR2 or Global Land Data Assimilation System (GLDAS) SM products (25 km x 25 km). This suggests that the L-band frequency (1.4 GHz) of the SMAP radiometer might lead to better performance regardless of spatial resolution (Chan et al., 2018). The greater penetration depth of the L-band could be also more representative of the ~20 cm depth of the gamma SM. In dense-forested areas with high vegetation canopy, it is extremely difficult to obtain accurate SM retrievals using the SMAP L-band and AMSR2 X-band frequencies. The AMSR2 X-band SM product over the Deciduous broadleaf forest and Mixed forest regions are typically masked with the data quality flag. In non-forested regions with bare ground or low vegetation canopy, the L-band SM performs better than X-band because the L-band frequency can partly penetrate low vegetation canopy while the higher-frequency X-band experiences greater attenuation (Kim et al., 2018; Jackson & Schmugge, 1991).

In the Deciduous broadleaf forest and Mixed forest classes, the operational gamma SM had a poorer agreement with SMAP SM than with NLDAS-2 SM, which agrees with previous validation studies of passive microwave SM products, including the SMAP radiometer. A known limitation of passive microwave soil moisture retrievals is that dense vegetation canopy over the soil surface reduces the sensitivity of the relationship between emissivity and SM (Jackson & Schmugge, 1991; Wigneron et al., 2003), even though the L-band microwave frequency yields relatively good results under vegetation covers relative to other, higher frequencies because of its higher penetration depth (Vittucci et al., 2016; Entekhabi et al., 2010). Due to the extremely high

625 optical depth of forests, there is little chance of reliably estimating SM conditions. For forest
626 types, Chan et al. (2016) found larger biases and *ubRMSD* between SMAP and in-situ SM
627 measurements at core validation sites (CVS), relative to other land cover types.

628 While SMAP SM has a wet bias in forest areas, there is no bias between operational
629 gamma SM and NLDAS-2 SM due to land cover. Considering that NLDAS-2 Mosaic SM is
630 estimated based on a physical land surface model (Koster & Suarez, 1996), it is likely that
631 gamma SM is less affected by vegetation effects than passive microwave (SMAP and AMSR2)
632 SM. The airborne gamma radiation technique depends on historical data to establish the
633 relationship between gamma count rates and SM and determine a standardized gamma count rate
634 at 35% gravimetric SM values for each calibration flight line (Carroll, 1980; 2001; Jones and
635 Carroll, 1983). This suggests that the vegetation effect on airborne gamma radiation observations
636 is minimal. Change in vegetation conditions by season are also minor because most gamma SM
637 observations – to estimate antecedent SM prior to soil freezing – are measured in late fall (e.g.
638 October or November) (Carroll, 2001). For these reasons, the gamma SM appears to be reliable
639 in forested regions and has the potential to be used beyond its operational estimates of SWE.
640 However, further investigation is still required to determine how gamma fluxes from the soil are
641 attenuated by vegetation characteristics (e.g. type, height, and density) and how much the
642 attenuation impacts SM estimates (Woods 1965; Schetselaar & Rencz, 1997; Ahl and Bieber,
643 2010).

644 Previous studies typically evaluated airborne gamma radiation SM with ground-based
645 SM observations. With an average of 25 samples gravimetric SM measurements per flight line,
646 Carroll (1981) and Jones and Carroll (1983) found airborne gamma SM had strong agreement

(R^2 = 0.87 and 0.84, *RMSD* = 3.2 and 3.9%, respectively). The airborne gamma radiation technique is considered to be a reliable method to estimate areal mean SM measurements.

No previous studies have compared gamma SM observations to satellite-based active and passive microwave or LSM SM, even though there are a series of satellite-based microwave sensors (e.g. SSM/I, AMSR-E/2, ASCAT, SMOS, and SMAP) and numerous evaluation studies since the early 1980s (e.g., Al-Yaari et al., 2014; Babaeian et al., 2019; Mladenova et al., 2014; Kim et al., 2018; Xia et al., 2014). This may be due to the operational mission of the airborne gamma program. As mentioned earlier, the airborne gamma radiation SM data collected by the NOAA NWS's Airborne Gamma Radiation Snow Survey Program is intended primarily to estimate SWE, not SM itself, and to provide the SWE data to the RFCs for use in the snowmelt flood forecasts. In light of the gamma radiation SM performance forests, gamma SM may help estimate SM in forested-dominated regions; one of the current challenges in the SM remote sensing community. As an independent asset, the airborne gamma radiation SM dataset can be utilized to evaluate current and future SM products from various satellites and land surface models to improve hydrological models.

6.2 Evaluation of SWE

The SMAP-updated gamma SWE agreement with satellite SWE is better than the previous findings by Tuttle et al. (2018). Tuttle et al. (2018) compared the operational gamma SWE to AMSR-E SWE estimates over the Northern Great Plains from 2002 to 2011. Their correlation coefficient (0.36) and *RMSD* (43 mm) is relatively poor compared to the SMAP-updated gamma SWE results and even the operational SWE. This may be due to different study periods between the two studies (2002-2011 versus 2015-2018). Their statistics could include a few erroneous SWE values during 2009 and 2011 when there were snowmelt floods. The

improved agreement of the SMAP-updated SWE with in-situ SWE, satellite microwave SWE, and GlobSnow SWE suggest that a portion of the error in operational gamma SWE caused by antecedent SM can be reduced using this proposed method.

Compared to the operational gamma SWE, the SMAP-updated SWE has better agreement with the limited available datasets including in-situ, satellite-based SSMIS, and GlobSnow assimilated SWE, but positive biases with in-situ and SSMIS SWE (10.4% and 11.8% respectively). Carroll and Schaake Jr (1983) also found that the airborne gamma SWE data tend to overestimate the ground-based data by approximately 10%. This may be due to the airborne gamma radiation method detecting water in all phases, including ground ice, standing water, and superimposed SM in the soil surface (Carroll, 2001), which might not be included in SWE observations from ground samples and snow stations. A snow pillow measures only the mass of the overlaying snowpack (Goodison et al., 1981) and has inherent limitations because the heat exchange between the snow and soil is disrupted, likely causing SWE underestimation (Bland et al., 1997). The current study suggests the method improves gamma SWE estimates but further validation with purposefully designed in-situ SWE measurements is needed.

6.3 Limitations

When the linear regression model between operational airborne gamma SM and SMAP SM was developed, the residual errors (ε_i) for each flight line were included in the model, assuming that the errors reflect the physical properties of the land surface within each line footprint (e.g. soil properties, elevation, slope, and inner spatial heterogeneity) (Clark et al., 2011). A residual analysis conducted with land surface characteristics (clay percentage, saturated hydraulic conductivity, and mean elevation and slope) to identify physical properties related to the errors and to assess the appropriateness of the model did not find any statistically significant

693 relationships. Carroll and Carroll (1989b) found that gamma SWE is systematically
694 underestimated when large SWE variability occurs within a flight footprint. Because the gamma
695 technique principles, measuring water mass by attenuation, are the same for SM and SWE, it
696 possible that SM variability could cause gamma SM to be underestimated. High-resolution soil
697 properties and SM-related variables (e.g. land surface temperature / Sentinel-1 SAR backscatter)
698 could be used to understand spatial heterogeneity impacts and to improve the operational gamma
699 SM methodology (Das et al., 2019).

700 A well-known issue when validating gridded satellite products with in-situ (or different
701 platform) measurements is the difference in spatial scales between the observations and the
702 ability of the sub-grid scale measurements to capture the variability within the satellite footprint
703 (Gruber et al., 2013; Colliander et al., 2017). Tuttle et al. (2018) noted that SWE spatial
704 variability affects the gamma versus satellite SWE comparison because of the different spatial
705 scales for the gamma footprint and the satellite pixel. The different observation scales may
706 contribute to the residual errors in the linear regression model between the gamma and SMAP
707 SM. The gamma SM lines often comprise parts of multiple SMAP pixels. The weighted mean
708 SMAP SM was found for the given flight footprint. However, the weighted mean SM is derived
709 from Tb observations that are partly from outside of the flight line footprint, thus introducing
710 representativeness errors into the linear model. Further studies are required to identify physical
711 characteristics that might be related to the residual errors in the model.

712 There may be temporal differences between airborne gamma radiation observations and
713 the satellite and model products in this study for SM and SWE comparisons. The gamma flight
714 overpass times range from 9 AM to 6 PM while the sun-synchronous SMAP, AMSR2, and
715 SSMIS sensors have constant local overpass times. Recognizing that SM has diurnal changes

(Jackson, 1973), the linear regression model between the operational airborne gamma and SMAP SM could be improved if the measurement time of the gamma flight data were known and the comparison included only those observations where measurement times were similar. It is also possible that this approach would improve if NLDAS-2 SM were used instead of SMAP SM because hourly NLDAS-2 SM values are available (Xia et al., 2015).

The different representative depths among the SM data sources also add error. The passive microwave sensors measure surface SM from the top few centimeters, with a depth that varies with the amount of soil moisture and its distribution (Njoku and Kong, 1977; Escorihuela et al., 2010). The L-band SMAP SM captures approximately the top 5 cm of the soil (O'Neill et al., 2018; McColl et al., 2017) whereas the X-band AMSR2 penetration depth is close to 1 cm (Bindlish et al., 2017) because lower-frequency microwave radiation generally penetrates soil and vegetation canopy more effectively than higher-frequency bands (Jackson & Schmugge, 1991). However, airborne gamma SM is derived from a larger depth range than the penetration depth of any current passive microwave satellite instrument (Carroll, 2001) with 91% of the gamma flux emitted from the upper 10 cm of the soil, and 96% from the upper 20 cm (Zotimov, 1968; Jones and Carroll, 1983). While the different sensors' representative depths are not dissimilar, the modest difference in representative depths could still cause errors, especially during dynamic wetting or drying (e.g., right after rainfall events).

7 Conclusion

In this study, a linear regression method was developed to improve operational airborne gamma SWE estimates in non-forested regions by updating the fall baseline SM using the SMAP enhanced SM product. Based on limited comparisons, the SMAP-updated SWE improves agreement with satellite and in-situ SWE observations. This preliminary study identified the

need to further test the approach as well as opportunities to improve the approach using higher-resolution/evolving independent products. For example, the Copernicus Sentinel-1 Synthetic Aperture Radar (SAR) provides 1-km C-band backscatter data. Because the SAR backscatter is directly related to surface SM condition, the Sentinel-1 SAR-based information could improve antecedent SM estimates over the gamma flight lines. However, current satellite SM observations offer little value for improving the gamma estimates in forested areas. In densely vegetated regions SM from LSMs, applied using this study's approach, could improve the operational gamma SWE regardless of land cover type. In the United States, snowmelt flood predictions are challenged by limited ground observations and rely heavily on the airborne gamma SWE product which is also used to support the operational SNODAS product. This study shows that the typical SWE corrections are on the order of 10 mm. Thus, the soil moisture corrections would be most important for regions having shallow snowpacks and snowmelt-driven flooding that is highly sensitive to modest SWE differences. Finally, gamma SWE estimates also serve as independent SWE measurements that are useful for evaluating satellite and modeled SWE products. An updated airborne gamma SWE with reduced errors will better support the evaluation of SWE products from current and future satellite missions and regional/global land surface or climate models.

Acknowledgments

We would like to thank the four anonymous reviewers and the RSE editorial team including Drs. Menghua Wang and Tim McVicar for taking their time to provide constructive comments that improve this paper. The authors gratefully acknowledge support from NASA Water Resources Applied Sciences Program (NNX15AC47G). We thank Simon Kraatz (UNH) for constructive discussions; Mike Cosh (USDA), Pedro Restrepo, Mike DeWeese, and Brian

Connelly (NOAA NCRFC) for their comments at the early stage of this research through our NASA RRB project. We are grateful to all who contributed to the data sets used in this study. The airborne gamma radiation survey SM and SWE data are available from the NOAA NWS NOHRSC website (http://www.nohrsc.noaa.gov/snowsurvey/). The SMAP Enhanced L3 Radiometer Global Daily 9 km EASE-Grid Soil Moisture, Version 2 (ID: R16000) were downloaded from the Earth Observing System Data and Information System (EOSDIS) (https://earthdata.nasa.gov/). The SSMIS brightness temperature data (Version 2) are freely available from the NASA National Snow and Ice Data Center website (https://nsidc.org/data/NSIDC-0032). The GlobSnow SWE data are available at http://www.globsnow.info/swe/. The in-situ SCAN SWE are also available from NRCS National Water and Climate Center (https://www.wcc.nrcs.usda.gov). The weekly ground snow survey SWE data are available on request from the USACE St. Paul District.

References

Ahl, A., Bieber, G., 2010. Correction of the attenuation effect of vegetation on airborne gamma-ray spectrometry data using laser altimeter data. Near Surf. Geophys. 8(4), 271-278.

Akbar, R., Short Gianotti, D., McColl, K. A., Haghighi, E., Salvucci, G. D., Entekhabi, D., 2018. Hydrological storage length scales represented by remote sensing estimates of soil moisture and precipitation. Water Resour. Res. 54(3), 1476-1492.

Al-Yaari, A., Wigneron, J.P., Ducharne, A., Kerr, Y.H., Wagner, W., De Lannoy, G., Reichle, R., Al Bitar, A., Dorigo, W., Richaume, P., Mialon, A., 2014. Global-scale comparison of passive (SMOS) and active (ASCAT) satellite based microwave soil moisture retrievals with soil moisture simulations (MERRA-Land). Remote Sens. Environ. 152, 614-626.

Armstrong, R., Knowles, K. Brodzik, M. Hardman, M., 1994. DMSP SSM/I-SSMIS pathfinder daily EASE-grid brightness temperatures. Version 2. NASA National Snow Ice Data Center Distributed Active Archive Center: Boulder, CO, USA. [accessed on 1 March, 2019]

Armstrong, R. L., Chang, A. Rango, A. Josberger, E., 1993. Snow depths and grain-size relationships with relevance for passive microwave studies. Ann. Glaciol., 17, 171-176

Armstrong, R.L.; Brodzik, M.J., 2001. Recent northern hemisphere snow extent: A comparison of data derived from visible and microwave satellite sensors. Geophys. Res. Lett. 28, 3673–3676.

Babaeian, E., Sadeghi, M., Jones, S. B., Montzka, C., Vereecken, H., & Tuller, M., 2019. Ground, Proximal and Satellite Remote Sensing of Soil Moisture. Rev. Geophys.

Barrett, A. P., 2003. National operational hydrologic remote sensing center snow data assimilation system (SNODAS) products at NSIDC (p. 19). Boulder, CO: National Snow and Ice Data Center, Cooperative Institute for Research in Environmental Sciences.

Bergeron, J. M., Trudel, M. Leconte, R., 2016. Combined assimilation of streamflow and snow water equivalent for mid-term ensemble streamflow forecasts in snow-dominated regions. Hydrol. Earth Syst. Sci., 20(10), 4375-4389. doi:10.5194/hess-20-4375-2016

Bilskie, J., 2001. Soil Water Status: Content and Potential. Campbell Scientific, Inc., Logan, UT

Bindlish, R., Cosh, M. H., Jackson, T. J., Koike, T., Fujii, H., Chan, S. K., ... & Collins, C. H., 2018. GCOM-W AMSR2 soil moisture product validation using core validation sites. IEEE J. Sel. Top. Appl. Earth Obs. Remote Sens. 11(1), 209-219. DOI: 10.1109/JSTARS.2017.2754293

Bland, W. L., Helmke, P. A. Baker, J. M. 1997. High-resolution snow-water equivalent measurement by gamma-ray spectroscopy. Agr. Forest Meteorol., 83(1-2), 27-36

Brodzik, M. J. 2014, F17 vs. F13 SWE Regression. Available online: http://cires1.colorado.edu/~brodzik/F13-F17swe/ [accessed on 27 March 2019].

Burnash, R. J. C., 1995, The NWS river forecast system–catchment modeling, in Computer Models of Watershed Hydrology, edited by V. P. Singh, pp. 311–366, Water Resour. Publ., Littleton, Colo.

Carroll, T. R., 1981. Airborne soil moisture measurement using natural terrestrial gamma radiation. Soil Sci. 132(5), 358-366.

Carroll, T., 2001. Airborne Gamma Radiation Snow Survey Program: A User's Guide, Version 5.0. National Operational Hydrologic Remote Sensing Center (NOHRSC), Chanhassen, 14

Carroll S. S. & Carroll T. R., 1989a. Effect of forest biomass on airborne snow water equivalent estimates obtained by measuring terrestrial gamma radiation. Remote Sens. Environ. 27(3), 313–319.

Carroll S. S., & Carroll T. R., 1989b. Effect of uneven snow cover on airborne snow water equivalent estimates obtained by measuring terrestrial gamma radiation. Water Resour. Res. 25 (7):1505–1510.

Carroll, T. R., Schaake Jr, J. C., 1983. Airborne snow water equivalent and soil moisture measurement using natural terrestrial gamma radiation. In Optical Engineering for Cold Environments (Vol. 414, pp. 208-214). International Society for Optics and Photonics.

Chan, S., Bindlish, R., O'Neill, P., Njoku, E.G., Jackson, T.J., Colliander, A., Chen, F., Bürgin, M., Dunbar, S., Piepmeier, J., Yueh, S., Entekhabi, D., Cosh, M., Caldwell, T., Walker, J., Wu, X., Berg, A., Rowlandson, T., Pacheco, A., McNairn, H., Thibeault, M., MartínezFernández, J., González-Zamora, Á., Seyfried, M., Bosch, D., Starks, P., Goodrich, D., Prueger, J., Palecki, M., Small, E., Calvet, J.-C., Crow, W., Kerr, Y., 2016. Assessment of the SMAP level 2 passive soil moisture product. IEEE Trans. Geosci. Remote Sens. 54 (8), 4994–5007. DOI:10.1109/TGRS.2016.2561938

Chan, S. K., Bindlish, R., O'Neill, P., Jackson, T., Njoku, E., Dunbar, S., ... & Colliander, A., 2018. Development and assessment of the SMAP enhanced passive soil moisture product. Remote Sens. Environ. 204, 931-941.

Chang, A., Foster, J. Hall, D. K., 1987. Nimbus-7 SMMR derived global snow cover parameters. Ann. Glaciol., 9(1), 39-44

Channan, S., Collins, K., Emanuel, W. R., 2014. Global mosaics of the standard MODIS land cover type data. University of Maryland and the Pacific Northwest National Laboratory, College Park, Maryland, USA, 30.

Cho, E., Jacobs, J. M., Tuttle, S. E., Schroeder, R., Olheiser, C., 2018. Improvement of airborne gamma radiation snow water equivalent estimations with spaceborne soil moisture observations, Proceedings of the 75th Annual Eastern Snow Conference: 5-8 June 2018, NOAA Center for Weather and Climate Prediction, College Park, Maryland, USA

Cho, E., Jacobs, J.M. and Vuyovich, C., 2019. The value of long-term (40 years) airborne gamma radiation SWE record for evaluating three observation-based gridded SWE datasets by seasonal snow and land cover classifications. Water Resour. Res. https://doi.org/10.1029/2019WR025813

Cho, E., Moon, H., Choi, M., 2015. First assessment of the advanced microwave scanning radiometer 2 (AMSR2) soil moisture contents in Northeast Asia. J. Meteorol. Soc. Jpn., 93(1), 117-129. https://doi.org/10.2151/jmsj.2015-008.

Cho, E., Tuttle, S. E., Jacobs, J. M., 2017. Evaluating Consistency of Snow Water Equivalent Retrievals from Passive Microwave Sensors over the North Central US: SSM/I vs. SSMIS and AMSR-E vs. AMSR2. Remote Sens. 9(5), 465.

Clark, M. P., Hendrikx, J., Slater, A. G., Kavetski, D., Anderson, B., Cullen, N. J., ... & Woods, R. A., 2011. Representing spatial variability of snow water equivalent in hydrologic and land-surface models: A review. Water Resour. Res. 47(7).

Clow, D. W., Nanus, L., Verdin, K. L., Schmidt, J., 2012. Evaluation of SNODAS snow depth and snow water equivalent estimates for the Colorado Rocky Mountains, USA. Hydrol. Process. 26(17), 2583-2591.

Colliander, A., Jackson, T.J., Bindlish, R., Chan, S., Das, N.N., Kim, S., Cosh, M.H., Dunbar, R.S., Dang, L., Pashaian, L., 2017. Validation of SMAP surface soil moisture products with core validation sites. Remote Sens. Environ. 191, 215–231.

Dai, L., Che, T., Wang, J., Zhang, P., 2012. Snow depth and snow water equivalent estimation from AMSR-E data based on a priori snow characteristics in Xinjiang, China. Remote Sens. Environ. 127, 14-29.

Das, N., D. Entekhabi, S. Dunbar, M. J. Chaubell, A. Colliander, S. Yueh, T. Jagdhuber, F. Chen, W. T. Crow, P. E. O'Neill, J. Walker, A. Berg, D. Bosch, T. Caldwell, M. Cosh, C. H. Collins, E. Lopez-Baeza, and M. Thibeault. 2019. The SMAP and Copernicus Sentinel 1A/B microwave active-passive high resolution surface soil moisture product, Remote Sens. Environ. 233. 111380. https://doi.org/10.1016/j.rse.2019.111380

Derksen, C., LeDrew, E., Walker, A., Goodison, B. 2000. Influence of sensor overpass time on passive microwave-derived snow cover parameters. Remote Sens. Environ. 71, 297–308.

Derksen, C., Walker, A., Goodison, B., 2005. Evaluation of passive microwave snow water equivalent retrievals across the boreal forest/tundra transition of western Canada. Remote Sens. Environ. 96(3-4), 315-327.

De Roo, A. P., Gouweleeuw, B., Thielen, J., Bartholmes, J., Bongioannini-Cerlini, P., Todini, E. Bates, P.D., Horritt, M., Hunter, N., Beven, K., 2003. Development of a European flood forecasting system. Intl. J. River Basin Management 1(1), 49-59

Dobson, M.C., Ulaby, F.T., Hallikainen, M.T., El-rayes, M., 1985. Microwave dielectric behavior of wet soil-Part II: dielectric mixing models. IEEE Trans. Geosci. Remote Sens. GE-23, 35-46.

886 Dong, J., Crow, W. T., & Bindlish, R. (2018). The error structure of the SMAP single and dual
887 channel soil moisture retrievals. *Geophysical Research Letters*, 45(2), 758-765.
888 Durand, M., Gatebe, C., Kim, E., Molotch, N., Painter, T., Raleigh, M., Sandells, M., Vuyovich,
889 C., 2019. NASA SnowEx Science Plan: Assessing approaches for measuring water in
890 Earth's seasonal snow, Version 1.6, [accessed on March 27, 2019] https://goo.gl/sFkxHc.
891 Ek, M. B., Mitchell, K. E., Lin, Y., Rogers, E., Grunmann, P., Koren, V., ... & Tarpley, J. D.,
892 2003. Implementation of Noah land surface model advances in the National Centers for
893 Environmental Prediction operational mesoscale Eta model. J. Geophys. Res.
894 Atmos., 108(D22).
895 Entekhabi, D., Njoku, E. G., O'Neill, P. E., Kellogg, K. H., Crow, W. T., Edelstein, W. N., ... &
896 Kimball, J., 2010. The Soil Moisture Active Passive (SMAP) mission. Proc. IEEE
897 98 (5), 704–716. DOI: 10.1109/JPROC.2010.2043918
898 Escorihuela, M.J., Chanzy, A., Wigneron, J.P., Kerr, Y.H., 2010. Effective soil moisture
899 sampling depth of L-band radiometry: a case study. Remote Sens. Environ. 114,
900 995–1001
901 Foster, J.L., Sun, C., Walker, J.P., Kelly, R., Chang, A., Dong, J., Powell, H., 2005. Quantifying
902 the uncertainty in passive microwave snow water equivalent observations. Remote Sens.
903 Environ. 2005, 94, 187–203.
904 Fournier, S., Reager, J. T., Lee, T., Vazquez-Cuervo, J., David, C. H., & Gierach, M. M., 2016.
905 SMAP observes flooding from land to sea: The Texas event of 2015. Geophys. Res.
906 Lett., 43(19), 10-338.
907 Glynn, J. E., Carroll, T. R., Holman, P. B., & Grasty, R. L., 1988. An airborne gamma ray snow
908 survey of a forested covered area with a deep snowpack, Remote Sens. Environ., 26(2),
909 149-160.
910 Goodison, B. E., Ferguson, H. L., & McKay, G. A., 1981. Measurement and data
911 analysis. Handbook of snow, 191-274.
912 Grasty, R., 1982. Direct snow-water equivalent measurement by air-borne gamma-ray
913 spectrometry. J. Hydrol., 55(1-4), 213-235.
914 Gruber, A., Dorigo, W. A., Zwieback, S., Xaver, A., & Wagner, W., 2013. Characterizing
915 coarse-scale representativeness of in situ soil moisture measurements from the
916 International Soil Moisture Network. Vadose Zone J. 12(2).
917 Hedrick, A., Marshall, H. P., Winstral, A., Elder, K., Yueh, S., & Cline, D., 2015. Independent
918 evaluation of the SNODAS snow depth product using regional-scale lidar-derived
919 measurements. The Cryosphere, 9(1), 13-23.
920 Imaoka, K., Kachi, M., Kasahara, M., Ito, N., Nakagawa, K., & Oki, T., 2010. Instrument
921 performance and calibration of AMSR-E and AMSR2. International Archives of the
922 Photogrammetry, Remote Sensing and Spatial Information Science, 38(8), 13-18.
923 Ishizaki, A., Sanada, Y., Mori, A. Imura, M., Ishida, M., Munakata, M., 2016. Investigation of
924 snow cover effects and attenuation correction of gamma ray in aerial radiation
925 monitoring. Remote Sens. 8(11), 892
926 Jackson, R. D., 1973. Diurnal Changes in Soil Water Content During Drying 1. Field soil water
927 regime, (fieldsoilwaterr), 37-55.
928 Jackson, T. J., Schmugge, T. J., 1991. Vegetation effects on the microwave emission of
929 soils. Remote Sens. Environ. 36(3), 203–212.
930 Jones, W. K., & Carroll, T. R., 1983. Error analysis of airborne gamma radiation soil moisture
931 measurements. Agric. Meteorol. 28(1), 19-30.

Kelly, R., 2009. The AMSR-E snow depth algorithm: Description and initial results. J. Remote Sens. Soc. Jpn,, 29(1), 307-317

Kelly, R. E., Chang, A. T., Tsang, L., Foster, J. L., 2003. A prototype AMSR-E global snow area and snow depth algorithm. IEEE Trans. Geosci. Remote Sens. 41(2), 230-242.

Kim, H., & Lakshmi, V., 2019. Global Dynamics of Stored Precipitation Water in the Topsoil Layer from Satellite and Reanalysis Data. Water Resour. Res., 55(4), 3328-3346.

Kim, H., Parinussa, R., Konings, A. G., Wagner, W., Cosh, M. H., Lakshmi, V., Zohaib, M., Choi, M., 2018. Global-scale assessment and combination of SMAP with ASCAT (active) and AMSR2 (passive) soil moisture products. Remote Sens. Environ. 204, 260-275.

Koike, T., 2013. Description of the GCOM-W1 AMSR2 Soil Moisture Algorithm, Technical Report–Description of the GCOM-W1 Level 1R and Level 2 Algorithms. Japan Aerospace Exploration Agency (JAXA) Earth Observation Research Center, pp. 8.1–8.13 NDX-120015A, Chapter 8.

Koster, R. D., Guo, Z., Yang, R., Dirmeyer, P. A., Mitchell, K., & Puma, M. J. (2009). On the nature of soil moisture in land surface models. Journal of Climate, 22(16), 4322-4335.

Koster, R. D., Suarez, M. J., 1996. Energy and water balance calculations in the Mosaic LSM. NASA Tech. Memo. 104606, Vol. 9, 60 pp. [Available online at http://gmao.gsfc.nasa.gov/pubs/docs/Koster130.pdf.]

Lawston, P. M., Santanello, J. A., & Kumar, S. V. (2017). Irrigation signals detected from SMAP soil moisture retrievals. Geophys. Res. Lett., 44(23).

Liang, X., Lettenmaier, D. P. Wood, E. F., Burges, S. J., 1994. A simple hydrologically based model of land surface water and energy fluxes for GCMs, J. Geophys. Res., 99, 14,415–14,428, doi:10.1029/94JD00483.

Liu, Y., Weerts, A., Clark, M., Hendricks Franssen, H. J., Kumar, S., Moradkhani, H., ... & Van Velzen, N., 2012. Advancing data assimilation in operational hydrologic forecasting: progresses, challenges, and emerging opportunities. Hydrol. Earth Syst. Sci. 16(10), 3863-3887. doi:10.5194/hess-16-3863-2012

Loew, A., 2008. Impact of surface heterogeneity on surface soil moisture retrievals from passive microwave data at the regional scale: the upper Danube case. Remote Sens. Environ. 112 (1), 231–248.

Luojus, K., Pullianen, J., Takala, M., Lemmetyinen, J., Kangwa, M., Eskelinen, M., et al., 2014. GlobSnow-2 Final Report, *Global Snow Monitoring for Climate Research, European Space Agency*, http://www.globsnow.info/docs/GlobSnow_2_Final_Report_release.pdf.

Ma, H., Zeng, J., Chen, N., Zhang, X., Cosh, M. H., & Wang, W. (2019). Satellite surface soil moisture from SMAP, SMOS, AMSR2 and ESA CCI: A comprehensive assessment using global ground-based observations. Remote Sens. Environ. 231, 111215. doi:10.1016/j.rse.2019.111215

Mladenova, I. E., Jackson, T. J., Njoku, E., Bindlish, R., Chan, S., Cosh, M. H., Holmes, T.R.H., de Jeu, R.A.M., Jones, L., Kimball, J., Paloscia, S., Santi, E., 2014. Remote monitoring of soil moisture using passive microwave-based techniques—Theoretical basis and overview of selected algorithms for AMSR-E. Remote Sens. Environ. 144, 197-213.

Mote, T. L., Grundstein, A. J., Leathers, D. J., & Robinson, D. A., 2003. A comparison of modeled, remotely sensed, and measured snow water equivalent in the Northern Great Plains. Water Resour. Res., 39(8), 1209. https://doi.org/10.1029/2002WR001782

977 McColl, K. A., Alemohammad, S. H., Akbar, R., Konings, A. G., Yueh, S., Entekhabi, D., 2017.
978 The global distribution and dynamics of surface soil moisture. Nat. Geosci. 10(2), 100.
979 Mishra, A., Vu, T., Veettil, A. V., & Entekhabi, D. (2017). Drought monitoring with soil
980 moisture active passive (SMAP) measurements. J. Hydrol., 552, 620-632.
981 Njoku, E. G., Kong, J. A., 1977. Theory for passive microwave remote sensing of near-surface
982 soil moisture. J. Geophys. Res. 82 (20) (July).
983 O'Neill, P. E., Chan, S. Njoku, E. G. Jackson, T., Bindlish. R., 2018. SMAP Enhanced L3
984 Radiometer Global Daily 9 km EASE-Grid Soil Moisture, Version 2. Boulder, Colorado
985 USA. NASA National Snow and Ice Data Center Distributed Active Archive Center.
986 doi: https://doi.org/10.5067/RFKIZ5QY5ABN.
987 Owe, M., De Jeu, R.A.M., Holmes, T.R.H., 2008. Multi-sensor historical climatology of satellite
988 derived global land surface moisture. J. Geophys. Res.: Atmos. 113:F1 F01002.
989 http://dx.doi.org/10.1029/2007JF000769
990 Painter, T. H., et al., 2016. The Airborne Snow Observatory: Fusion of scanning lidar, imaging
991 spectrometer, and physically-based modeling for mapping snow water equivalent and
992 snow albedo. Remote Sens. Environ. 184, 139-152. doi:10.1016/j.rse.2016.06.018
993 Peck, E. L., Bissell, V. C., Jones, E. B., & Burge, D. L., 1971. Evaluation of snow water
994 equivalent by airborne measurement of passive terrestrial gamma radiation. Water
995 Resour. Res. 7(5), 1151–1159.
996 Peck, E. L., Carroll, T. R., VanDemark, S. C., 1980. Operational aerial snow surveying in the
997 United States/Etude de neige aérienne effectuée aux Etats Unis. Hydrol. Sci. J., 25(1),
998 51–62
999 Pulliainen, J., Hallikainen, M., 2001. Retrieval of regional snow water equivalent from space-
1000 borne passive microwave observations. Remote Sens. Environ. 75(1), 76-85.
1001 Pulliainen, J., 2006. Mapping of snow water equivalent and snow depth in boreal and sub-arctic
1002 zones by assimilating space-borne microwave radiometer data and ground-based
1003 observations. Remote Sens. Environ. 101(2), 257-269.
1004 Rannie, W., 2015. The 1997 flood event in the Red River basin: Causes, assessment and
1005 damages. Canadian Water Resources Journal / Revue canadienne des ressources
1006 hydriques, 41(1-2), 45-55. doi:10.1080/07011784.2015.1004198
1007 Schroeder, R., Jacobs, J.M., Cho, E., Olheiser, C., DeWeese, M., Connelly, B., Cosh, M., Jia, X.,
1008 Vuyovich, C., Tuttle. S.E., 2019. Comparison of satellite passive microwave with
1009 modeled snow water equivalent estimates in the Red River of the North basin. IEEE J.
1010 Sel. Top. Appl. Earth Obs. Remote Sens. doi: 10.1109/JSTARS.2019.2926058
1011 Schetselaar E.M., Rencz A.N., 1997. Reducing the effects of vegetation cover on airborne
1012 radiometric data using Landsat TM data. Int. J. Remote Sens. 18, 1503–1515.
1013 Stadnyk, T., Dow, K., Wazney, L., Blais, E.-L., 2016. The 2011 flood event in the Red River
1014 Basin: causes, assessment and damages. Can. Water Resour. J., 41(1-2), 65-73
1015 Takala, M., Luojus, K., Pulliainen, J., Derksen, C., Lemmetyinen, J., Kärnä, J. P., Koskinen, J.,
1016 & Bojkov, B., 2011. Estimating northern hemisphere snow water equivalent for climate
1017 811 research through assimilation of space-borne radiometer data and ground-based
1018 812 measurements. Remote Sens. Environ. 115(12), 3517-3529.
1019 Tait, A. B., 1998. Estimation of snow water equivalent using passive microwave radiation
1020 data. Remote Sens. Environ. 64(3), 286-291.
1021 Todhunter, P. E., 2001. A hydroclimatological analysis of the Red River of the North snowmelt
1022 flood catastrophe of 1997. JAWRA J. Am. Water Resour. Assoc. 37(5), 1263-1278

Tuttle, S. E., Cho, E., Restrepo, P. J., Jia, X. Vuyovich, C. M., Cosh, M. H., and Jacobs, J. M., 2017. Remote Sensing of Drivers of Spring Snowmelt Flooding in the North Central U.S, 21-45. doi:10.1007/978-3-319-43744-6_2

Tuttle, S. E., Jacobs, J. M., Vuyovich, C. M., Olheiser, C., Cho, E., 2018. Intercomparison of snow water equivalent observations in the Northern Great Plains. Hydrol. Process. 32(6), 817-829.

Vittucci, C., Ferrazzoli, P., Kerr, Y., Richaume, P., Guerriero, L., Rahmoune, R., Vaglio Laurin, G., 2016. SMOS retrieval over forests: exploitation of optical depth and tests of soil moisture estimates. Remote Sens. Environ. 180, 115–127.

Vuyovich, C., Jacobs, J. M., 2011. Snowpack and runoff generation using AMSR-E passive microwave observations in the Upper Helmand Watershed, Afghanistan. Remote Sens. Environ., 115(12), 3313-3321. doi:10.1016/j.rse.2011.07.014

Vuyovich, C. M., Jacobs, J. M., Hiemstra, C. A., Deeb, E. J., 2017. Effect of spatial variability of wet snow on modeled and observed microwave emissions. Remote Sens. Environ. 198, 310-320. doi:10.1016/j.rse.2017.06.016

Wang, J. R., Mcmurtrey, J. E., III, Engman, E. T., Jackson, T. J., Schmugge, T. J., Gould, W. I., et al., 1982. Radiometric measurements over bare and vegetated fields at 1.4-GHz and 5-GHz frequencies. Remote Sens. Environ. 12(4), 295–311.

Wazney, L., Clark, S.P., 2015. The 2009 flood event in the Red River Basin: Causes, assessment and damages. Can. Water Resour. J. / Revue canadienne des ressources hydriques, 41(1-2), 56-64. doi:10.1080/07011784.2015.1009949

Wigneron, J. P., Calvet, J. C., Pellarin, T., Van de Griend, A. A., Berger, M., & Ferrazzoli, P., 2003. Retrieving near-surface soil moisture from microwave radiometric observations: current status and future plans. Remote Sens. Environ. 85(4), 489-506.

Wood, E. F., Lettenmaier, D., Liang, X., Nijssen, B., & Wetzel, S. W., 1997. Hydrological modeling of continental-scale basins. Annual Review of Earth and Planetary Sciences, 25(1), 279-300.

Woods F.W., Hough W.A., O'Nea D. Barnett J., 1965. Gamma ray attenuation by Loblolly pine wood: An investigation of integral counting. For. Sci. 11, 341–345.

Xia, Y., Sheffield, J., Ek, M. B., Dong, J., Chaney, N., Wei, H., Meng, J., Wood, E. F., 2014. Evaluation of multi-model simulated soil moisture in NLDAS-2. J. Hydrol. 512, 107-125. https://doi.org/10.1016/j.jhydrol.2014.02.027

Xia, Y., Ek, M. B., Wu, Y., Ford, T., Quiring, S. M., 2015. Comparison of NLDAS-2 simulated and NASMD observed daily soil moisture. Part I: Comparison and analysis. J. Hydrometeorol. 16(5), 1962-1980. https://doi.org/10.1175/JHM-D-14-0096.1

Zhang, R., Kim, S., & Sharma, A., 2019. A comprehensive validation of the SMAP Enhanced Level-3 Soil Moisture product using ground measurements over varied climates and landscapes. Remote Sens. Environ. 223, 82–94. doi:10.1016/j.rse.2019.01.015

Zotimov, N. V., 1968. Investigation of a method of measuring snow storage by using the gamma radiation of the earth. Sov. Hydrol. Sel. Pap., (3), 254-266.

Zwieback, S., Colliander, A., Cosh, M. H., Martínez-Fernándezj, J., McNairn, H., Starks, P. J., ... & Berg, A., 2018. Estimating time-dependent vegetation biases in the SMAP soil moisture product. Hydrol. Earth Syst. Sci., 22(8), 4473-4489.

List of Figure Captions

Figure 1. An example time series of satellite/model soil moisture (SMAP enhanced products in this figure) within the given flight line footprint and NOAA operational gamma soil moisture along with daily rainfall and air temperature in 2016 to 2017 from a North Dakota Agricultural Weather Network (NDAWN) station at Mooreton, ND. The ND440 flight line was flown over the Mooreton station. The increase in SMAP soil moisture in December was due to early snowmelt from 26 to 30, November. The errors of the SMAP product (ubRMSE < 0.04 m3/m3) meet the mission performance criteria from previous studies (Chen et al., 2018; Colliander et al., 2018).

Figure 2. Land cover map of the study area of the north-central and eastern United States and southern Canada with the NOAA airborne gamma flight lines surveyed from 2015 to 2018 (N = 574, blue lines with cyan borders) with River Forecasting Center (RFC) boundaries (black lines) along with U.S. states and Canadian province boundaries (gray lines). The land cover map is from Global Mosaics of the Moderate Resolution Image Spectroradiometer (MODIS) land cover type product (MCD12Q1).

Figure 3. SM difference maps for NLDAS-2, SMAP, and AMSR2 for the years 2015 to 2017. SM differences are calculated between the date of the fall baseline gamma flights and the date of the last SM observation prior to freezing onset. A past 5-day composite SM map was used to eliminate spatial gaps.

Figure 4. Comparison of NOAA airborne gamma soil moisture with (a, b) Phase 2 of the North American Land Data Assimilation System (NLDAS-2) Mosaic SM, (c, d) Soil Moisture Active Passive (SMAP) Level 3 enhanced soil moisture, and (e, f) Advanced Microwave Scanning Radiometer 2 (AMSR2) SM within the given flight line footprints with/without the SM values from forested areas.

Figure 5. (a) Boxplots of SMAP SM at original (operational) and latest available dates and original and updated gamma SM for entire flight lines in the non-forested region from 2015 to 2017, along with (b) the corresponding original and updated gamma SWE. (a) The small circles are individual SM data (no meaning for a spread in the horizontal direction) and the larger circles are outliers. The bold line within each colored box is median, and the upper and bottom sides of the box are the upper (75%) and lower (25%) quantiles of the data. (b) The width of the leaf-shape boxplot shows the relative amount of the SWE data at that magnitude.

Figure 6. Histogram of (a) changes in SMAP SM and (b) NOAA airborne gamma SWE from the date of the baseline fall gamma flights to the date immediately before winter freeze-up

Figure 7. Comparison between operational and SMAP-updated NOAA airborne gamma snow water equivalent with (a, b) satellite-based snow water equivalent from Special Sensor Microwave Imager Sounder (SSMIS) and (c, d) ESA GlobSnow assimilation SWE within the given flight line footprint. The points are colored by day of year (DOY).

Figure 8. (a) Time series of in-situ SWE measurements with the operational and SMAP-updated gamma SWE at the Glacial Ridge Station, Minnesota (ID: 2050) from the Soil Climate Analysis Network (SCAN) and (b) agreement between the in-situ SWE and the operational and SMAP-updated gamma SWE. The red points in both plots indicate the operational gamma SWE, while the green points indicate SMAP-updated gamma SWE.

Figure 9. (a) Time series of in-situ SWE measurements with the operational and SMAP-updated gamma SWE at three sites (Baldhill, ND, Orwell, MN, and Traverse, MN) from the United States Army Corps of Engineers (USACE) and (b) agreement between the in-situ USACE SWE and the operational and SMAP-updated gamma SWE. The red points in both plots indicate the operational gamma SWE, while the green points indicate SMAP-updated gamma SWE.